Title
Investigation of in vivo Metabolism in Hepatic Carcinomas

Author
Shihadih, Diyala Sharli

Publication Date
2022

Peer reviewed|Thesis/dissertation

Investigation of in vivo Metabolism in Hepatic Carcinomas

By

Diyala Shihadih

A dissertation submitted in partial satisfaction of the

requirements for the degree of

Doctor of Philosophy

in

Metabolic Biology

in the

Graduate Division

of the

University of California, Berkeley

Committee in Charge:

Professor Andreas Stahl, Chair
Professor Daniel Nomura
Professor Marc Hellerstein
Professor Kunxin Luo

Spring 2022

Abstract

Investigation of in vivo Metabolism in Hepatic Carcinomas

By

Diyala Shihadih

Doctor of Philosophy in Metabolic Biology

University of California, Berkeley

Professor Andreas Stahl, Chair

Metabolic reprogramming is a common feature of cancers with many showing specific alterations in both micro and macronutrient metabolism. In this study we evaluate the utility of bioluminescent technology in evaluating the metabolism of liver cancers *in vivo*. We assess both nutrient uptake and nutrient sensing probes to establish the handling and/or concentrations of lipids, glucose, nicotinamide riboside, iron, copper, and ROS in both healthy mice and tumor bearing mice. Our studies showed promise for the lipid, copper, iron, and ROS probes and were able to measure metabolic differences in copper and lipid metabolism between our different cancer models.

We evaluated both hepatocellular carcinoma (HCC) and intrahepatic cholangiocarcinoma (ICC) models that were established through a hydrodynamic injection. Our bioluminescent study revealed a fatty acid uptake phenotype in our ICC model, but not our HCC models, which is a rare but increasingly documented phenotype. Classical cancer lipid metabolism focuses on the upregulation of de novo lipogenesis concomitant with a decreased dependence on exogenous fatty acids. Increased expression and activity of fatty acid synthase (FASN), the rate-limiting enzyme involved in de novo lipogenesis, is required for the survival and proliferation of many tumor cells, including hepatocellular carcinoma (HCC). Another study previously demonstrated that ICC development is insensitive to FASN deprivation. Our observation that ICC maintains robust fatty acid uptake rates suggests a role of exogenous fatty acids for the growth of ICC. Fatty acid transport proteins (FATPs), now classified as solute transporter family 27 (Slc27a1-6), are major transmembrane proteins for LCFA uptake and FATP2 and -5 are robustly expressed in the liver, FATP5 being liver specific. Using genetic manipulation and in vivo bio-imaging techniques, we measured the growth of ICC in an FATP5 knock out mouse model over time. Loss of FATP5 significantly impaired ICC growth indicating that tumor growth is dependent on exogenous fatty acid uptake. This was replicated using a knockdown system in both our ICC and HCC models, and only in ICC did we see a growth impairment. We also performed a survival experiment to see how long the growth effect in ICC was maintain. Over the course of 32 week, only three out of 7 mice grew robust tumor and when assayed for lipid uptake and metabolizing genes, two showed upregulation of FASN.

Metabolomic were also performed to determine the fate and function of these fatty acids comparing ICC, HCC, and non-tumorous liver. Our data showed a robust increase in free fatty acids, structural, signaling lipids, and acyl-carnitines suggesting a differential handling of exogenous versus endogenous fatty acids. We attempted to follow up on the increased levels of acyl-carnitines, which are implicated in beta-oxidation and energy generation. We treated mice with CPT1 inhibitor etomoxir and saw no significant growth effect. While it is obvious ICC is dependent on fatty acid uptake, and the inhibition of uptake is able to prevent tumor growth, the differential handling of the downstream fatty acids is more complex. In sum, this study has identified FATP5 as a therapeutic target for the treatment of ICC and potentially other liver cancers dependent on protein mediated exogenous fatty acid uptake.

Table of Contents

Dedication

This dissertation is dedicated to my family. This work is for you.

To my maternal grandparents, Sido Yaser and Teta Nawal, who left their home, immigrated to a new country with all their children, and sacrificed so much in the process. I hope I have fulfilled your wildest dreams. To my paternal grandparents, Sido Yousef and Teta Therese, who have been with me in spirit through this journey. I hope my work and who I've become makes you proud.

To my parents, Sharli and Maha, who have been my biggest supporters. You have instilled in me a love for education and showed me that anything is possible if I put my mind to it. You have sacrificed so much to give us every opportunity and experience you didn't get, and I hope I have made you proud with my choices. Love you so much and can't wait until you're with me as I walk down the stage and become your "doctor".

To my sisters, Deema and Danya, who have brought me so much joy and laughter. Your achievements bring me so much pride and I hope mine do the same. I've had to watch both of you grow and develop while I've been away at different universities, and I haven't always been there, but I'm so proud of the people you have become. I hope to be the nerdy sister and aunt of your dreams. This dissertation is also for you, and I won't make you call me Dr. Diyala.

To the rest of my extended family, all my aunts, uncles, and cousins. Your constant love and support has pushed me through the last few years, and I couldn't have finished without all of you by my side. You ground me and remind me that educational pursuits do not start and end in the academy but are for everyone to access and benefit from.

This dissertation is the culmination of so many people's love, knowledge, and hard work, and will only continue from here.

Acknowledgments

First, I'd like to acknowledge everyone who helped me in completing the work written about in this dissertation. My mentor Andreas Stahl who has supported my work and taught me how to be an effective scientist. My entire dissertation committee, Daniel Nomura, Marc Hellerstein, and Kunxin Luo, for their support in completing this dissertation. All of the collaborators who contributed to and supported my investigations into in vivo cancer metabolism including but not limited to Xin Chen, Elena Goun, Christopher Chang, Daniel Nomura, and Marc Hellerstein. I'd also like to thank all of the core facilities that have maintained the machinery used to complete this work helped me develop the skills needed to perform the experiments necessary to substantiate my hypotheses, specifically Steve Ruzin and Denise Schichnes of the Biological Imaging Facility.

I'd like to thank the entire Stahl lab for being my support system through the years. Ching Fang for always bringing happy energy to the lab and helping us with every aspect of lab maintenance and experimental design. Your mentorship, knowledge, and support will be missed. My cohort and bench mate Pete. Thank you for always being there to support me in whatever scientific venture I began and being part of my emotional support system as we both attempted the difficult task of achieving our PhDs. You are a fantastic scientist, and I cannot wait to see what you do next. Garrett for being the first person when you walk into the lab and always having something nice to say. You have been on this journey with us, and I look forward to your graduation as well. The rest of the Stahl lab, Xue, Lin, Irene, Amanda, and Kaitlyn, for being there to support the work and success of every member of the lab.

To all of my undergraduate mentees that have supported my work and taught me how to be a good mentor. You reminded me every day the impact we as scientists can have on the next generation and showed me how important is to not only research but teach. Your excitement and dedication in the lab motivated me to continue my work when I was tired and disillusioned.

Lastly, I'd like to thank John Matsui for being my science education mentor the past few years. Your support and teaching has helped me find my role in science. I will forever be grateful for giving me the chance to teach with you.

Chapter 1:
Novel Bioluminescent Imaging Techniques to Assess *in vivo* Metabolism

Summary

In this chapter, we will be evaluating and characterizing a total of six bioluminescent nutrient probes for *in vivo* use. The probes are designed to either measure nutrient uptake levels or static nutrient levels. We will characterize the in vivo kinetics of each probe and attempt to assess if we are generating biologically relevant and accurate measurements. All probes have been previously published on and assessed to varying degrees. We will offer an assessment of the viability of each probe for *in vivo* metabolic assessment.

If deemed viable, probes be tested in our bioluminescent tumor systems, which we will also outline in this chapter. Our three tumor systems are models for intrahepatic cholangiocarcinoma and hepatocellular carcinoma and are compatible with luciferin-based imaging probes in order either 1) to measure tumor burden over time using d-luciferin and 2) measure nutrient concentrations and fluxes in a noninvasive and longitudinal manner. Our goal is to not only assess the utility of bioluminescent nutrient probes but to also evaluate metabolic differences between our tumor types for further evaluation and pharmaceutical target development.

Introduction and Background

It is understood that many human diseases involve and are associated with abnormal alterations in metabolism. Perturbation of metabolism can alter cellular function and lead to disease, and disease states stemming from different causes can lead to metabolic alterations[1-3]. The core of metabolic research centers on the three major macronutrients, lipids, carbohydrates, and amino acids, but also includes small molecules, vitamins, and minerals. While most research starts *in vitro*, being able to quickly assess the status and levels of these micro and macronutrients *in vivo* is essential for validating and exploring the contributions of metabolism to disease to then move towards therapeutic target development with greater confidence.

Current techniques to assessing *in vivo* metabolism range from whole body respiration measurements using metabolic chambers [4] and NMR based imaging [5-7], which can be done at multiple timepoints throughout an experiment, to mass spectrometry based techniques which are end point measurements. While all provide important information about in vivo metabolism, few techniques are able to measure specific nutrient dynamics in both a longitudinal and noninvasive manner. Bioluminescence as a technique has high sensitivity because of its efficient photon production and the lack of background signal in a biological system, and is associated with relatively low costs, making it an attractive research tool [8,9].

The use of bioluminescent probes is long documented and different groups are exploring the utility and viability of different homologues of luciferase as a research tool for routine and specialized application. Many groups are specifically applying the technology to look at disease states both *in vivo* and *in vitro* [10-12]. The use of this technology in disease state metabolic assessment goes back to ex vivo studies that used luciferase to quantify the spatial distribution of ATP, lactate, and glucose in ex vivo section of tumors and nontumorous tissue using single photon microscopy [13]. Since then, *in vivo* bioluminescent technology has been used to measure tumor growth and metastasis, immune cell dynamics[14-16], transgene expression, infection, and other biological processes related to health and disease [17-31].

In this study, we will be utilizing firefly luciferase to explore metabolic phenotypes of different forms of liver cancer. The field of cancer research is ever growing as we add more complexity to our understanding of cancer transformation and progression [32]. One of the newer established hallmarks of cancer is aberrant metabolism [33-35], with the Warburg effect being the most well studied [36]. The Warburg effect describes a phenomenon where tumors become highly glycolytic, heavily relying on glucose uptake, and push glucose metabolism toward lactic acid production, termed aerobic glycolysis[37]. Aberrant metabolism, outside of glucose metabolism, includes the flux and dynamics of all macro and micronutrients in the system. Our study will focus on a few micro and macro nutrients in order to test the ability to quantify their levels or fluxes using bioluminescent technology.

Bioluminescent probes

We have classified the bioluminescent probes used in this study into two categories, nutrient uptake probes and nutrient sensing probes (**Fig. 1.1**). These probes are all based in a caged luciferin technology. Luciferin is the necessary substrate for luciferase in order to produce light. Using different techniques, molecules can be chemically attached to luciferin, in a reversable way, to prevent luciferase from acting on it. The way the luciferin is caged and uncaged determines what is being measured by the resulting bioluminescent signal.

Nutrient uptake probes are intended to measure the uptake rates of nutrients and the function of their associated transporter. There are two approaches that have been taken to develop these types of probes. The first is to attach luciferin to the nutrient of interest through a linker that auto hydrolyzes upon uptake into the cell. The fatty acid probe used in this study is designed in this method. The second is a dual probe approach. This is use for nutrients that will not function in a physiologically relevant manner if a large luciferin moiety is attached. This could be because of a transporter's high specificity, like the GLUT transporters. In this method, we have both a caged luciferin and a nutrient probe that has the ability to uncage the luciferin upon interaction. The technology is based on the biorthogonal reaction (Staudinger ligation), where the nutrient contains an azide group to uncage a pre-loaded caged luciferin in the system[38]. The glucose and nicotinamide riboside probes were designed in this manner.

Nutrient sensing probes are intended to measure the amount of a small molecule or metal that is in the system. This allows us to monitor the concentration and distribution of molecules of interest over time. In this method, the caged luciferin is liberated when it comes into contact with and reacts with a specific molecule[39]. In our study, the probes used sense peroxide, copper, and iron.

Lipids

Altered lipid metabolism plays a role in cancer growth and development[40]. While most research has focused on *de novo* lipogenesis, in recent years there is more focus on the role of lipid uptake in cancer development. As research progresses in this area, having more tools to measure fatty acid uptake rate *in vivo* will be indispensable.

Glucose

Cancer has long been established to be highly glycolytic. Glucose metabolism plays a huge role in cancer metabolism from energy generation to anabolic processes[41]. Glucose uptake is upregulated in cancers, usually seen by increased expression of GLUT transporters. Depending on tissue type, the main transporters of interest are GLUT 1, GLUT2 and GLUT3, and have been research as potential therapeutic targets[42-44]. A bioluminescent glucose uptake probe could be applied in the context of both tumor characterization and pharmaceutical development.

Nicotinamide riboside

Nicotinamide riboside (NR) is a dietary source of nicotinamide adenine dinucleotide (NAD). NAD+ is an essential cofactor in multiple redox reactions involved in energy production including glycolysis and is a substrate for different signaling enzyme[45]. Increased NAD levels are

seen in cancers to fuel growth[46,47]. Nicotinamide phosphoribosyltransferase (Nampt), a rate limiting step in NAD synthesis, is seen to be upregulated in certain cancers[48]. NAD and NAD production is implicated in cancer development and growth, but it is unclear the role of dietary sources of NAD. Nicotinamide riboside is also a commonly used supplement. Using the bioluminescent NR probe, one can investigate the role and uptake levels of dietary sources of NAD.

Copper

Copper is an essential trace metal involved in many biological processes. Copper is a part of many enzymes, used for its redox potential, and plays a role in angiogenesis cellular mechanisms and other signaling pathways. The dysregulation of copper homeostasis can lead to disruptions in cellular processes and disease[49,50]. Copper levels have been identified as a potential diagnostic and prognostic marker in cancer and as a therapeutic target[49,51]. Some studies have found elevated copper levels in tumor areas, the tumors themselves, and in the serum of cancer patients[49]. A bioluminescent copper detecting probe is a quick and easy way to assess copper levels in a tumor system to evaluate if dysregulated copper metabolism is contributing to tumorigenesis.

Iron

Iron is an essential trace metal necessary for many cellular processes including DNA synthesis, proliferation, cell cycle regulation, and the function of proteins and enzymes containing iron-sulphur clusters, some of which are involved in genomic stability and respiration. Excess iron can also have deleterious effects including promoting mutagenesis which can lead to tumor formation[52]. High dietary iron intake and diseases that lead to increased copper accumulation are associated with increased cancer risk [53]. Cancer cells have also seen to have an increased dependance on iron. Tumors reprogram their metabolism to increase iron uptake by upregulating key uptake proteins and decreasing the expression of iron efflux proteins. Iron is also a target for cancer therapy with researchers exploring iron chelators and molecules targeting iron uptake and transport machinery and as a cancer prognostic tool [54]. A bioluminescent iron sensing probe would allow researchers to quickly measure the quantity of iron in a tumor system to evaluate if increased copper levels are contributing to cancer growth and metabolism.

Reactive oxygen species (ROS)

Reactive oxygen species are highly reactive ions or molecules and are grouped into two groups, free oxygen radicals and non-radical ROS. Free oxygen radicals include nitric oxide, super oxides, and hydroxyl radicals, and non-radical ROS include singlet oxygen and hydrogen peroxide[55]. ROS is a byproduct of respiration and is generated in many areas of the cell including the mitochondria[56]. The most studied ROS in cancer are hydrogen peroxide and hydroxyl radicals. Cancers have long been observed to have increased ROS production and can lead to the activation of tumorigenic signaling and metabolic reprograming and can induce DNA mutation[56,57]. Excessive levels of ROS can also trigger cell death. The modulation of intracellular ROS has been exploited as an anti-cancer strategy [58]. The bioluminescent probe used in this study directly measures peroxide as an output for ROS.

Results

In an effort to identify novel in vivo imaging techniques to assess differences in metabolism in disease states, we characterized and tested a variety of available bioluminescent imaging probes in a liver cancer model adapted for in vivo imaging.

We established a bioluminescent tumor model in mice (**Fig. 1.2**). We coupled a hydrodynamic transduction mediated oncogene driven liver cancer system with bioluminescent technology to establish luciferase expressing tumor nodules, which allowed us to measure tumor burden and nutrient uptake in vivo.

To establish our two cancer models, we delivered the following oncogenes: constitutively activated Akt and notch receptor intracellular domain (NICD) to establish intrahepatic cholangiocarcinoma, and either constitutively activated Akt and Ras or constitutively activated Akt and cMet to establish hepatocellular carcinoma. These oncogenes are delivered with sleeping beauty transposase to stably integrate the oncogenes, creating stable oncogene driven tumor nodules. To couple this system with bioluminescent technology, we cloned a firefly luciferase gene into the Akt plasmid linking Akt and luciferase expression through an IRES. This system allowed us to establish tumor specific luciferase expression which, upon a standard 100ul (2mg/ml) luciferin i.p. injection, can be seen in ex-vivo images taken using an in vivo imaging system (IVIS) (**Fig. 1.3a**). This imaging system gives us a functional readout for tumor burden. To further test this system, we imaged both ICC and HCC tumor bearing mice once a week, starting 1 week post hydrodynamic injection, to measure in vivo tumor growth over the course of 7 weeks, at which time the mice were sacrificed due to tumor size (**Fig. 1.3b**). We saw a steady exponential growth rate over the course of the seven weeks starting at 3 weeks post injection, demonstrating that we can accurately measure tumor burden and growth rates using bioluminescent imaging.

As further validation of the bioluminescent signal, we attempted to establish the ICC tumor model both with and without sleeping beauty transposase to test for any potential background signal from unincorporated plasmid (**Fig. 1.3c**). We imaged the mice three time in the first week post injection and again at two weeks post injection. We saw a steady decline of the bioluminescent signal over the course of the first week in the group without sleeping beauty transposase and by 7 days post injection, there was no bioluminescent signal whereas the group with the transposase maintained a bioluminescent signal. This demonstrated that when we begin our routine imaging protocol at one week post injection, there should be no background bioluminescent signal from unincorporated plasmid obfuscating the data.

This model was used in conjunction with various bioluminescent probes to assess the metabolism of ICC in comparison to HCC. We were able to establish a lipid uptake phenotype in our ICC model that was not replicated in our HCC models using a previously validated bioluminescent free fatty acid (FFA-luc) [59,60]. Starting at one week post hydrodynamic injection, we imaged ICC and HCC (Akt-Ras) tumor bearing mice using both luciferin and FFA-luc (**Fig. 1.4a**). We waited 24 hours between luciferin and FAA-luc imaging to allow for the full decay of

luciferin to prevent the measurement of any residual bioluminescence. To get a proper readout of FFA uptake, in each imaging session we measured photon emission every 5 minutes for one hour and quantified and plotted for the maximal FFA uptake. We were able to measure uptake rates that increased over time in a similar pattern to our tumor growth rates. We normalized the FFA uptake at each time point by our luciferin measurement to get a read out for uptake rates proportional to tumor burden (**Fig. 1.4b)**. We observed that ICC consistently maintained fatty acid uptake levels higher than HCC upon full tumor establishment at 3 weeks post injection, with highly significant FFA uptake levels at seven weeks when we have high tumor burden (**Fig. 1.4c**). This experiment was replicated in a second HCC model (Akt-cMet) and again saw significantly lower fatty acid uptake rates at the seven-week post injection timepoint (**Fig. 1.4d**). It is important to note that in this system, there is no background bioluminescent signal. This allows for a greater dynamic range for measurement assuming the probe elicits a strong bioluminescent signal as we've observed with the FFA-luc probe. These data showed that we could indeed measure differences in metabolism using our bioluminescent tumor system.

We went on to validate and test other nutrient uptake bioluminescent probes in our system. We utilized two other nutrient uptake probes, nicotinamide riboside and glucose probes, that use a different technology than our bioluminescent free fatty acid. These probes are synthesized to "uncage" a preloaded caged luciferin upon uptake into cells [38] (**Fig. 1.1)**. Before testing the nutrient probes, we went on to validate the use of the caged luciferin probe (CLP) *in vivo* (**Fig. 1.5**). In previous studies, 1.5 mM in 100 uL PBS+0.1%BSA CLP was administered intravenously (i.v.). For imaging ease, we tested the same dosage of CLP through intraperitoneal (i.p.) injection compared to i.v. injection to assess if it was a viable administration route. While there was higher variability withing the i.p. injected group three hours post CLP injection, by 18 hours post injection when the nutrient probe is administered, the CLP levels between the two groups were comparable. For all following experiment, CLP was administered intraperitoneally.

First, we tested the nicotinamide riboside (NR) probe at 5 mM in PBS (100ul) through oral gavage. NR is a commonly used supplement and is implicate in NAD dependent metabolic processes including energy metabolism. We wanted to assess if we could detect changes in NR intestinal absorption before testing in a disease state. We used liver luciferase mice for the following experiments. First, we tested absorption in a fasted state (**Fig. 1.6a**). Mice were fasted overnight for 16 hours. At the end of the fast, mice were imaged for background CLP signal then the 100ul of the NR probe (5mM) in PBS was administered through oral gavage. Mice were imaged for one hour to measure NR uptake rates. This protocol was then repeated in fasted mice that were refed for two hours prior to NR administration (**Fig. 1.6b**). The area under each curve was measured to compare the uptake rates of each treatment group (**Fig. 1.6d**). We saw no change in NR intestinal uptake rates between the two groups. Another issue we ran into was the signal to noise ratio. The signal from the NR probe was only 2-3 fold higher than the CLP background signal, giving us a small detectable range. We were unable to measure changes in NR uptake using this probe, thus we did not test it in our cancer models.

The final nutrient uptake probe tested was the glucose probe. As done previously, we preinjected mice with 100 uL 1.5 mM CLP through intraperitoneal injection 16-18 hours prior to glucose probe administration. Mice were pre-imaged to establish background signal, and then 200ul 7.5 mM glucose probe in PBS+0.1%BSA was i.p. injected and mice were subsequently imaged to measure glucose uptake. We first tested the probe in liver luciferase mice, checking the kinetics of the probe during the first 15 minutes of imaging to verify we are seeing an increase in uptake over time, and for 15 starting at the 70 minutes post administration time point to look at the degradation of the glucose probe (**Fig. 1.7**). We saw a clear increase in signal during the first 15 minutes validating the probe is being taken up by the mice and measured, at most, a threefold increase in signal above background. We still saw a bioluminescent signal after 70 minutes putting into question the sensitivity of the probe. We then re-ran this experiment, this time imaging the mice for 30 minutes to establish a kinetic curve in the liver luciferase mice (**Fig. 1.8a**). We saw peak signal at 25 minutes post injection, after which the signal began to decline. At this peak signal, we measured a fivefold increase in signal above background.

With the kinetics of the probe in vivo established, we proceeded to test if the probe was behaving in a biologically relevant manner. We ran a competition assay by co-injecting D-glucose to test if the probe was diffusing into cells or being actively taken up through glut transporters (**Fig. 1.8b**). If the probe was being imported into the cell through GLUT transporters, we expected to see a decrease in the kinetic rate of the probe. We saw a modest attenuation of the uptake rate indicating that at least some of the probe was being taken up through transporters.

We proceeded to test the probe in our cancer models. We established both our ICC model and one of our HCC models (Akt-cMet). We imaged mice weekly to track tumor growth and once high tumor burden was established, we proceeded to image using the glucose probe following the same protocol as previously done (**Fig. 1.8c,d**). The day before glucose imaging was performed, we imaged the mice for tumor burden to be used for normalization of the glucose signal. The kinetic curve established through glucose imaging of our HCC model showed a strong peak in signal with a subsequent decline as expected. The imaging of our ICC model displayed a lower overall signal and did not have the expected signal peak. Instead, we see more of a consistent plateauing of the signal. Once the data was normalized to tumor burden, we saw a different kinetic curve for each tumor model. Our ICC model had an overall higher signal per quantity of tumor than HCC and had a flatter peak signal at 25 minutes post glucose injection. In contrast, the HCC model had a clear signal peak at 10 minutes post glucose injection. This data shows a potential difference in glucose uptake between our HCC and ICC models, but with the low sensitivity and lack of data established biological relevance of the probe, we did not continue imaging experiments using the glucose probe.

The next class of imaging probes we tested were nutrient sensing probes. These are caged luciferin probes that “uncage” when they react with a specific metal or small molecule [39] (**Fig. 1.1**) and have all been previously validated *in vivo*. All the following probes were tested in tumor bearing mice. Wild type mice were hydrodynamically injected to establish both our ICC

(Akt-NICD) and HCC (Akt-cMet) tumor models. These mice were imaged weekly to track the establishment and growth of the tumors. Once tumors were established and we reached high tumor burden, we imaged with the nutrient sensing probes to assess if we could image for differences in metabolism between the two models.

We first tested the copper probe by i.p. injecting a 100nmol of CCL-1 in 50 ul 1:1 PBS DMSO solution (**Fig. 1.9a**). These mice were imaged every 5 minutes for 45 minutes and the peak signal was used as our primary readout for copper content in our system. This readout was then normalized to tumor burden established by luciferin imaging. We first performed our imaging protocol in liver-luciferase mice to establish a baseline quantity of copper in nontumorous liver tissue. Then we imaged for copper levels in our ICC (Akt-NICD) and HCC (Akt-cMet) model systems. While both tumor systems showed slower copper levels than what was measured in the liver luciferase mice, the HCC model had significantly higher copper levels than the ICC model.

We went on to validate this observation using laser ablation inductively coupled plasma mass spectrometry (LA-ICP-MS) (**Fig. 1.9b,c**). Tumor bearing mice were monitored until full tumor burden was established, at which point they were euthanized, their livers were perfused with PBS, and snap frozen blocks of tumor laden liver tissue were made. LA-ICP-MS analysis revealed that ICC tumor nodules indeed had little to no copper when compared to the surrounding non-tumorous tissue as is seen in the pseudo-colored images. This confirmed that the copper imaging probe was giving an accurate readout of copper levels. Interestingly, the LA-ICP-MS data also uncovered a ring of high copper containing cells surrounding the tumor nodules as can be observed by both the two-dimensional images and 3-D surface plot. This observation was replicated in multiple samples. While we were unable to identify the copper containing cells, this showed that new information about cell metabolism can easily and accurately be gleaned from bioluminescent imaging and the subsequent follow-up experiments.

The last two nutrient sensing probes tested in our tumor systems were an iron sensing probe and a hydrogen peroxide sensing probe. The iron sensing probe was administered through i.p. injection, 25nmol per mouse in 100ul 1:4 DMSO:PBS. Mice were imaged every 5 minutes for a total of 45 minutes. Again, the peak signal was used as copper concentration readout. The mice were pre-imaged with luciferin to establish tumor burden 24 hours before copper imaging and a ratio of copper concentration to tumor burden was calculated to determine relative copper concentration in our tumor models (**Fig. 1.10**). No significant difference between our ICC and HCC model was measured using this probe.

The hydrogen peroxide probe is used as a read out of reactive oxygen species (ROS) levels (**Fig. 1.11**). As cancer is known to upregulate reactive oxygen species, we expected to see a high bioluminescent signal. We administered through i.p. injection 0.5umol of the PCL1 probe in 50 ul 1:1 DMSO:PBS solution. Mice were subsequently imaged every 5 minutes for 45 minutes. The peak signal was then normalized to tumor burden. As expected, we had a high ROS, Luciferin ratio demonstrating a strong bioluminescent signal from the PCL1 probe, but no difference was seen measured between our ICC (Akt-NICD) and HCC (Akt-cMet) models.

These studies show that we can indeed measure in vivo metabolism through bioluminescent technology and using the appropriate model and probe, we are able to detect difference in metabolism when comparing different disease states. The bioluminescent free fatty acid probe and copper probe both elucidated differences in metabolism between our HCC and ICC models, while the copper and ROS probes were shown to be viable for in vivo use though we saw no metabolic differences in our models. The current limitations of nutrient level and nutrient uptake measurements through novel bioluminescent technology are related to the sensitivity of the probes and if they are behaving in a physiologically relevant manner.

Discussion

In this chapter we attempted to test the efficacy and accuracy of bioluminescent imaging of metabolism *in vivo*. Currently, there are few methods to test in vivo metabolism in a noninvasive manner that allows for sequential measurements over time. Currently the tools at our disposal to measure in vivo metabolism are metabolic chambers to measure respiration rates[4], mass spectrometry based techniques including heavy water labeling [61-63] and use of isotopically labeled tracers [64,65], and NMR based imaging [5-7]. The use of a noninvasive method like bioluminescent imaging could provide researchers with a powerful tool to interrogate multiple levels of metabolism in the same system and to do so longitudinally without having to euthanize an animal to obtain data.

To this end, we tested a total of six probes, three nutrient uptake probes, and three nutrient sensing probes. Our primary goal was to test the viability, accuracy, and/or biological relevance of each probe. Our secondary goal was to then use these probes in a disease model, in this case one of our three cancer models, to characterize the metabolism of each system and test for differences between the cancer models. Before we were able to probe for metabolic differences in our tumor systems, we first had to establish and characterize a tumor system that allowed for bioluminescent imaging.

We coupled a hydrodynamic injection based tumor system [66] with bioluminescent technology but delivering a luciferase gene along with one of our oncogenes (Akt-IRES-Luciferase). Through this, we were able to characterize the growth pattern and rate of our tumor systems (**Fig.1.3**). We see a high bioluminescent signal started at one week post injection. This is all from stably integrated plasmid as when we inject our oncogene containing plasmids without sleeping beauty transposase, we have no bioluminescent signal at this timepoint. The subsequent light signal decreases and/or plateaus between week one and week three as tumors establish. After the third week, we start to see the signal increase as tumors begin to actively grow. This pattern of tumor growth beginning after three weeks post injection hold true for all tumor models used for our studies.

We used a total of three tumor models for this study, one ICC model and two HCC model. Our ICC model is established by delivering constitutively active Akt and Notch intracellular domain (NICD)[67]. We used two HCC models because our Akt-Ras system is a mixed tumor system where up to ten percent of the tumors established are ICC [68,69]. In the future, this is an interesting system to utilize to look at a non-heterogeneous system that might offer more translatable metabolic information. Our Akt-cMet system is a pure HCC model that does not establish any ICC nodules[70]. This gives us multiple comparisons when characterizing different metabolic phenotypes of each tumor type.

The first nutrient uptake probe we characterized and tested in our tumor systems was the free fatty acid probe [59] (**Fig. 1.4**). Aberrant lipid metabolism is a known feature of cancer metabolism. It is well documented that many cancers rely on de novo lipogenesis to replenish their lipid pools and there is more recent data that also points to maintained or increased levels

of fatty acid uptake as well [40]. Using our bioluminescent free fatty acid probe, we were able to measure the fatty acid uptake rates of our tumor models and found that fatty acid uptake levels are high in our ICC model in contrast to both of our HCC model which did not seem to be taking up a significant amount of fatty acid. We were also able to measure these uptake rates throughout the life of our tumors as imaging is noninvasive and can be done in a live anaesthetized mouse. This allowed us to accurately identify a differential lipid uptake phenotype that was not previously documented which we subsequently followed up on in chapter 2.

While our free fatty acid probe gave us accurate information about lipid fluxes in our tumor system and was sensitive enough to measure differences between our tumor systems, the second set of nutrient uptake probes were not as effective. Both the nicotinamide riboside probe and glucose probe used a different strategy to uncage luciferin upon the nutrient probe uptake. In this system, a caged luciferin is pre-injected to the mice and the nutrient probe has a moiety attached to it that will react with the caged luciferin and uncage it allowing luciferase to then act on free luciferin. This is done with nutrients that cannot have a large moiety, like luciferin, attached to them because they will not be appropriately taken up by their receptor and thus will not behave in a biologically relevant manner.

We first tested the administration route and kinetics of the caged luciferin probe (CLP) (**Fig. 1.5**). We found that we were able to i.p. inject his probe for ease of administration instead of an i.v. injection as was previously published. The main issue with the CLP was the high background signal. The probe is not very stable and will spontaneously uncage giving us a background signal. It is unclear what percentage of total probe uncages spontaneously and how much uncage probe is left in the system upon nutrient probe administration.

Both the NR and glucose probes were first tested in our liver luciferase mice before moving into our tumor systems if the probe seemed viable. With both the NR and glucose probes, the highest signal we were able to achieve in the liver luciferase mice was a threefold signal above background. This was concerning as this is not a large signal range in order to measure differences in metabolism between different treatment groups. First, we tested the NR probe (**Fig. 1.6**). NR is implicated in NAD^+ metabolism and its deregulation has been associated with metabolic disease including cancer [46]. We were unable to measure changes in NR uptake between our fasted and fasted-refed groups, so we did not proceed with this probe.

The glucose probe was tested next (**Fig. 1.7, Fig. 1.8**). We characterized the uptake kinetics of this probe in liver luciferase mice and saw the expected bell curve shape over time although we did not achieve a strong peak signal. We then tested if the probe was behaving in a biologically relevant manor by performing a competition assay using D-glucose, which would be a natural competitor for uptake through glucose transporters [38,71,72]. If the glucose probe was indeed being taken up by glucose transporters, we would see a decrease in signal upon co-injection with D-glucose. We saw a mild decrease in uptake rates. It was not conclusive whether this probe was diffusing into the cells or being taken up through the appropriate transporters. Nonetheless, we proceeded to test this probe in our tumor systems. Once again, the data

obtained from our ICC and HCC systems was inconclusive. We saw a difference in the probe kinetics, but we were unable to come to any conclusions about the glucose uptake rates in our tumor systems.

The next class of probes we tested were nutrient sensing probes. These probes are designed to measure the amount of nutrient in a system at the time of imaging. They are a form of caged luciferin that is designed to uncage upon reacting with a specific metal or small molecule. We tested a total of three nutrient sensing probes in our tumor systems, a copper sensing probe, an iron sensing probe, and a peroxide sensing probe. All three of these probes gave us a strong signal *in vivo*. While we did not measure a significant difference between our ICC and HCC models using the iron and peroxide probes, we did measure a significant difference using the copper probe.

The copper probe when tested in out ICC and HCC system showed a significant decrease of copper levels in our ICC system when compared to HCC (**Fig. 1.9**). To follow up and validate this observation, we performed LA-ICP-MS on perfused liver cancer samples. The results from the LA-ICP-MS analysis showed the ICC did indeed have significantly lower amount of copper. This is seen in the pseudo coloring of the images. While the surrounding nontumorous liver tissue is blue, signifying moderate copper levels, the tumor nodules are black, signifying little to no copper. We also stumbled upon an unusual observation through these follow ups. We observed a ring of high copper containing cells surrounding the tumor nodules. This was replicated across all the samples we tested. Copper has previously been implicated in cancer as both a cancer promoting and an anti-cancer molecule [50]. While we were unable to identify what these specifics copper containing cells are, this is a valid route for further follow-ups looking at copper's role in ICC development.

These tests all showed the viability of using bioluminescent imaging probes to investigate the metabolism of disease states in vivo. While not every probe we tested was viable, the probes that did show high specificity and sensitivity allowed us to easily and quickly evaluate various elements of metabolism in our tumor systems. These measurements gave us important information about the metabolism of our systems which allowed for more informed follow up experiments.

Figures

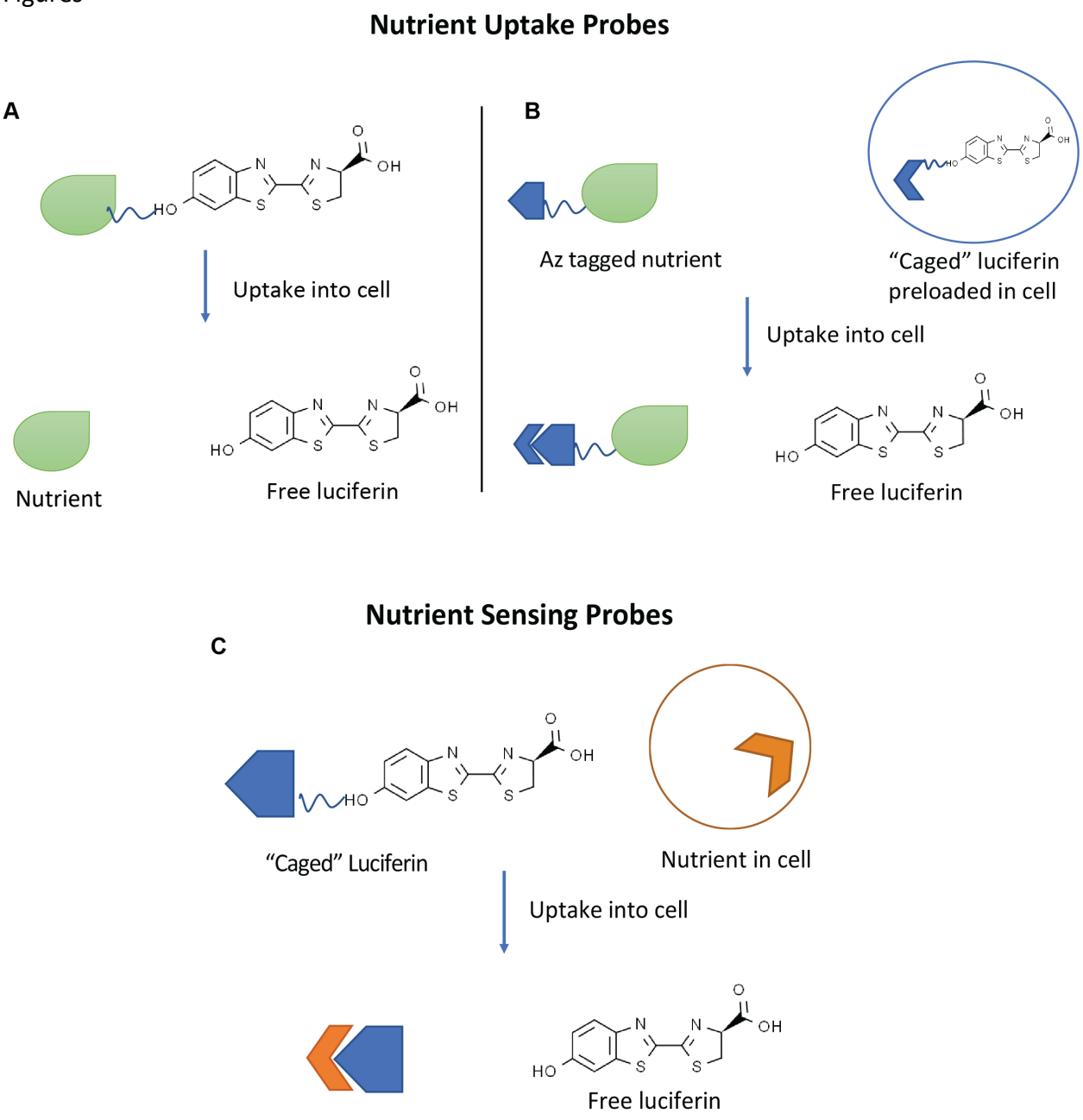

Figure 1.1. Classes of Bioluminescent Probes
Two classes of bioluminescent probes. The first designed to measure nutrient uptake with two design strategies (A) uses a single probe that uncages upon cellular uptake and (B) uses a dual uptake system where nutrient uptake uncages a preloaded caged luciferin probe. The second (C) is designed to measure nutrient concentrations. The probe releases luciferin upon reacting with a small molecule or metal intracellularly.

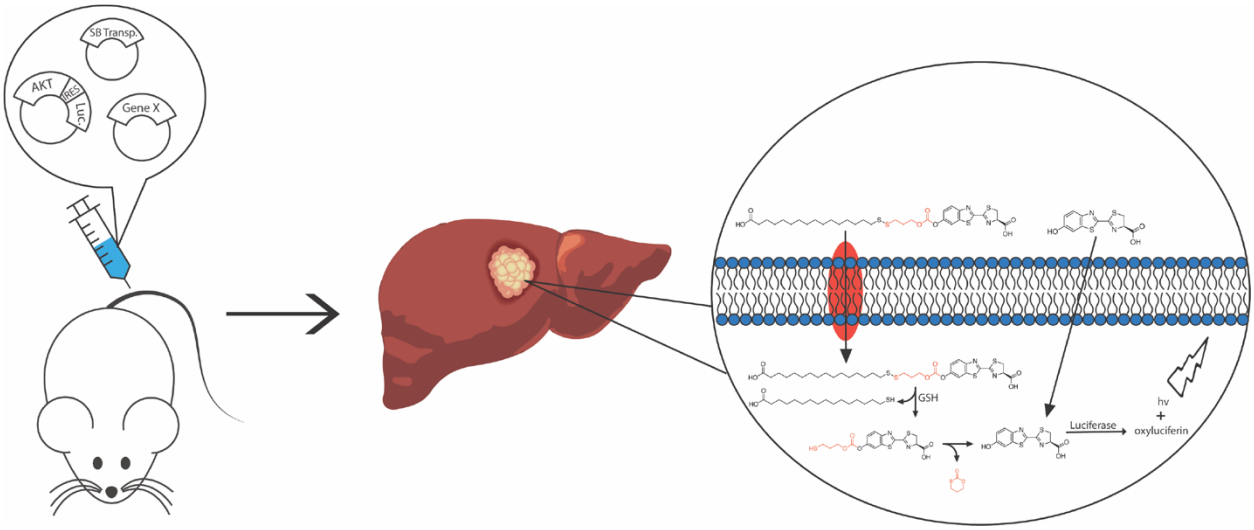

Figure 1.2. Tumor Model System
Our tumor system is established through a hydrodynamic injection coupled with bioluminescent technology. This establishes bioluminescent tumors that can produce light upon luciferin uptake or the uptake of bioluminescent probes.

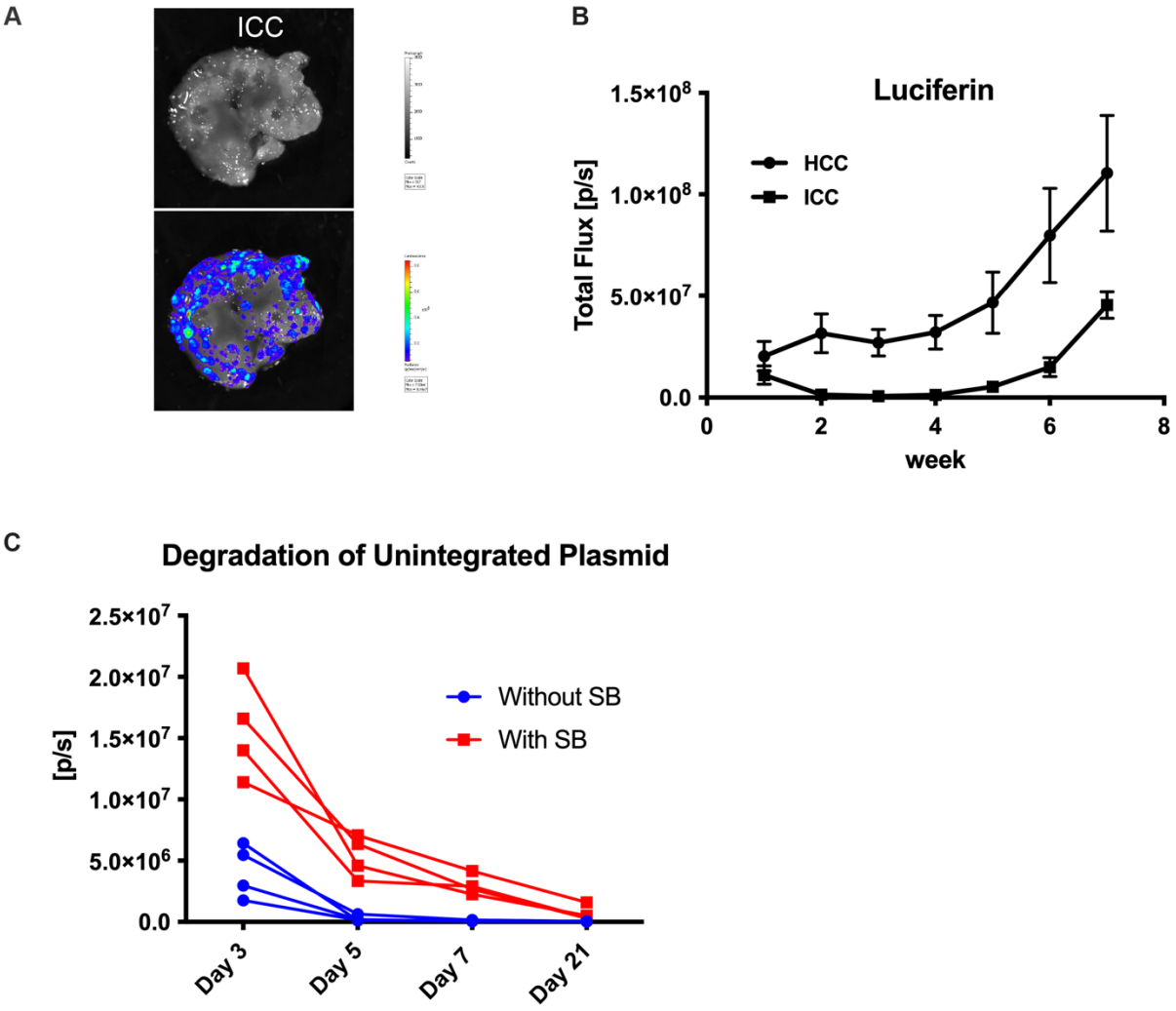

Figure 1.3. Tumor model validation
To validate our tumor model, we (B) tracked tumor growth over the course of 7 weeks and (B) took ex vivo images comparing the photo and bioluminescent signal overlay to visually determine if light was emanated only from tumor nodules. We measured the bioluminescent signal of hydrodynamically injected mice with and without sleeping beauty transposase to look at the rate of plasmid degradation

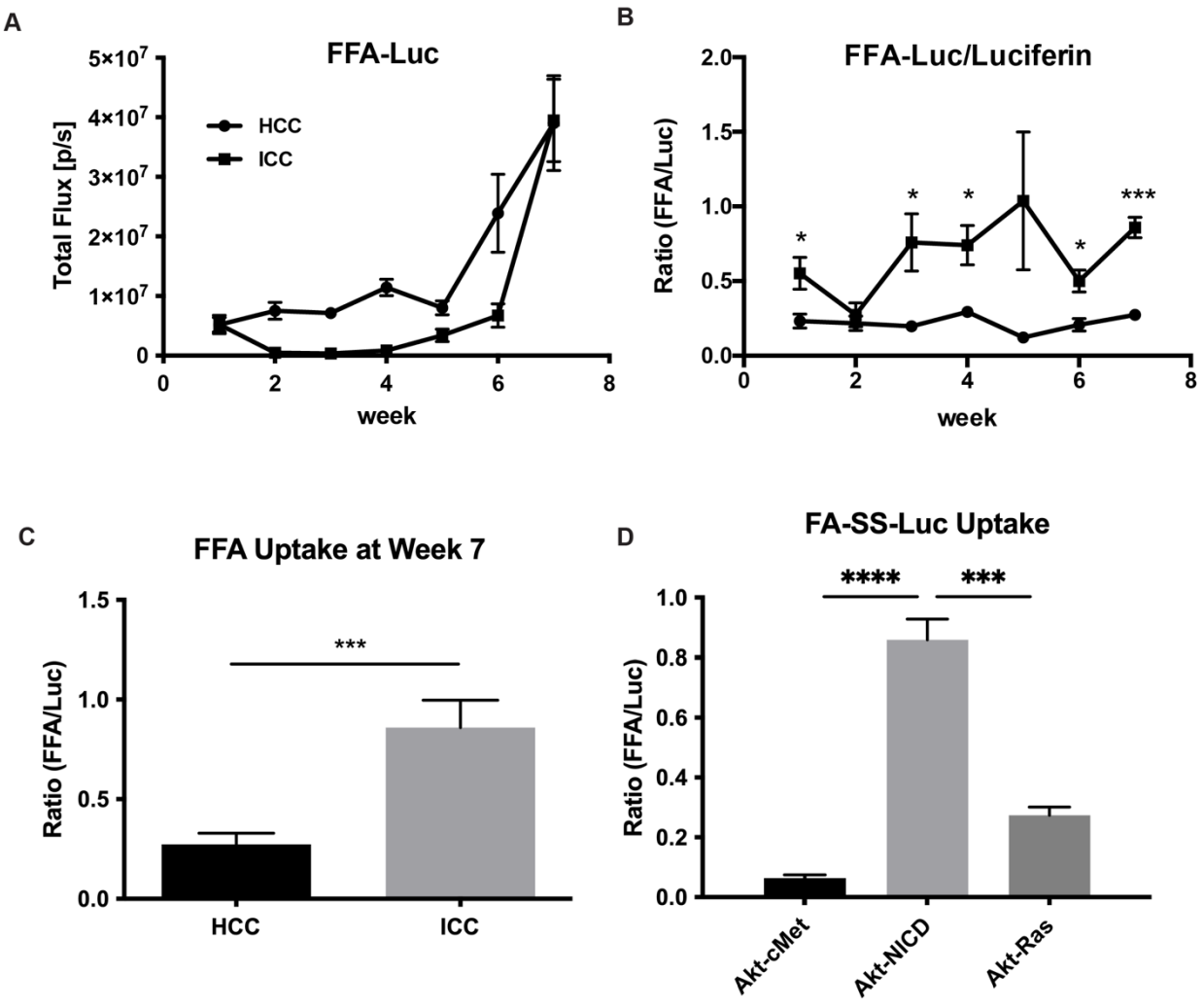

Figure 1.4. Fatty Acid Uptake

We measure (A) fatty acid uptake rates in ICC and HCC over the course of 7 weeks and (B) normalized uptake to tumor burden at each timepoint. (C) We saw significantly upregulated uptake rates in ICC and (D) this data was replicated using both out HCC models

A

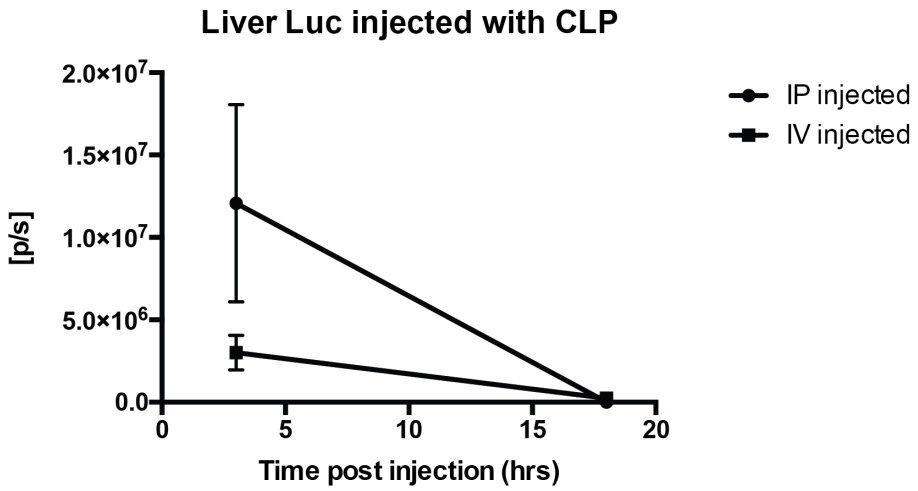
Liver Luc injected with CLP
2.0×10^7
1.5×10^7
1.0×10^7
5.0×10^6
0.0
[p/s]
0
5
10
15
20
Time post injection (hrs)
IP injected
IV injected

B

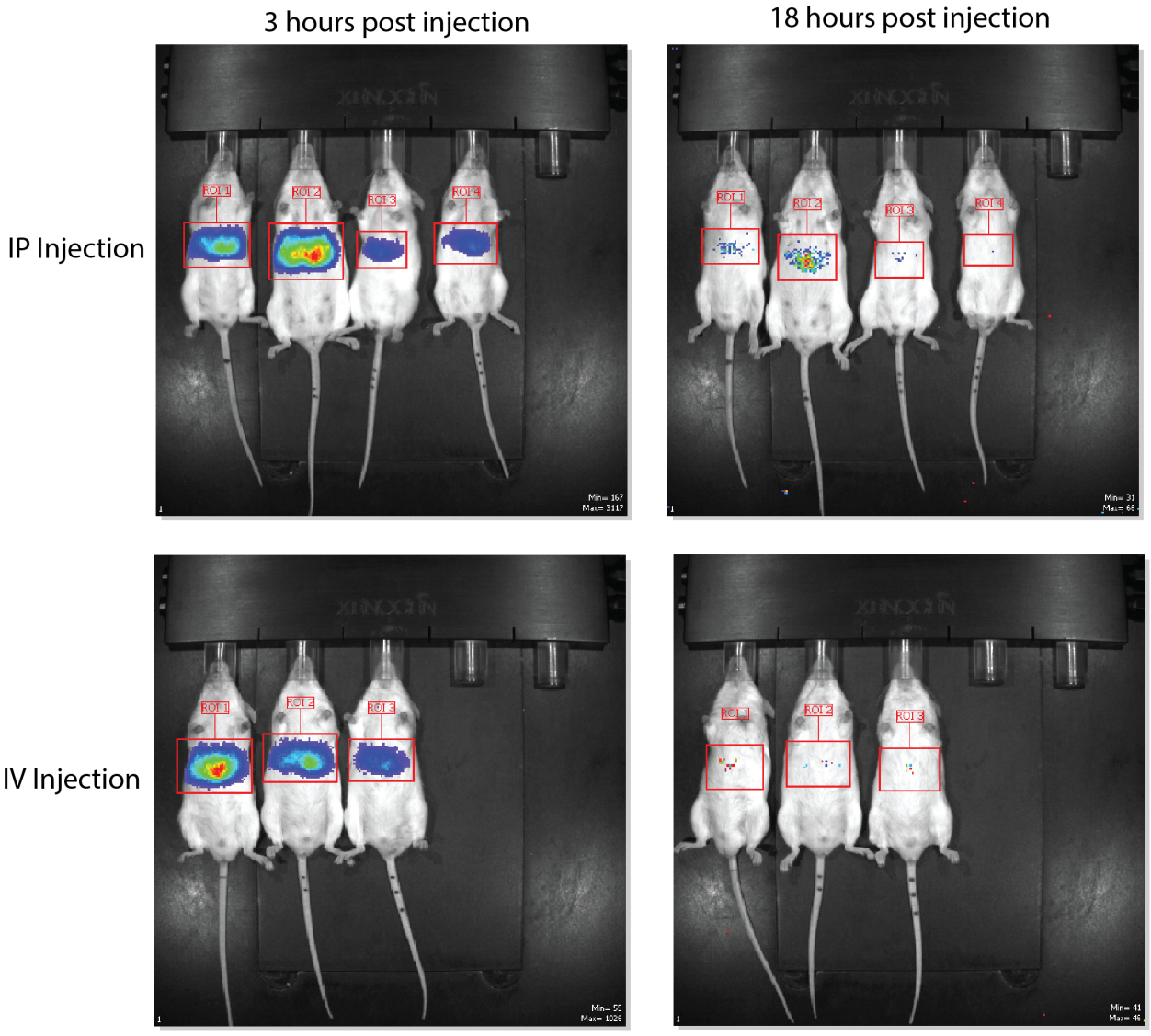
3 hours post injection
18 hours post injection
IP Injection
IV Injection

Figure 1.5. CLP Administration Validation
In order to use our dual uptake probes, we needed to validate the route of administration of out caged luciferin probe (CLP). We (A) compared i.p. and i.v. injections of our CLP at 3 hours and 18 hours post injection and (B) included the bioluminescent images of the mice at this timepoints.

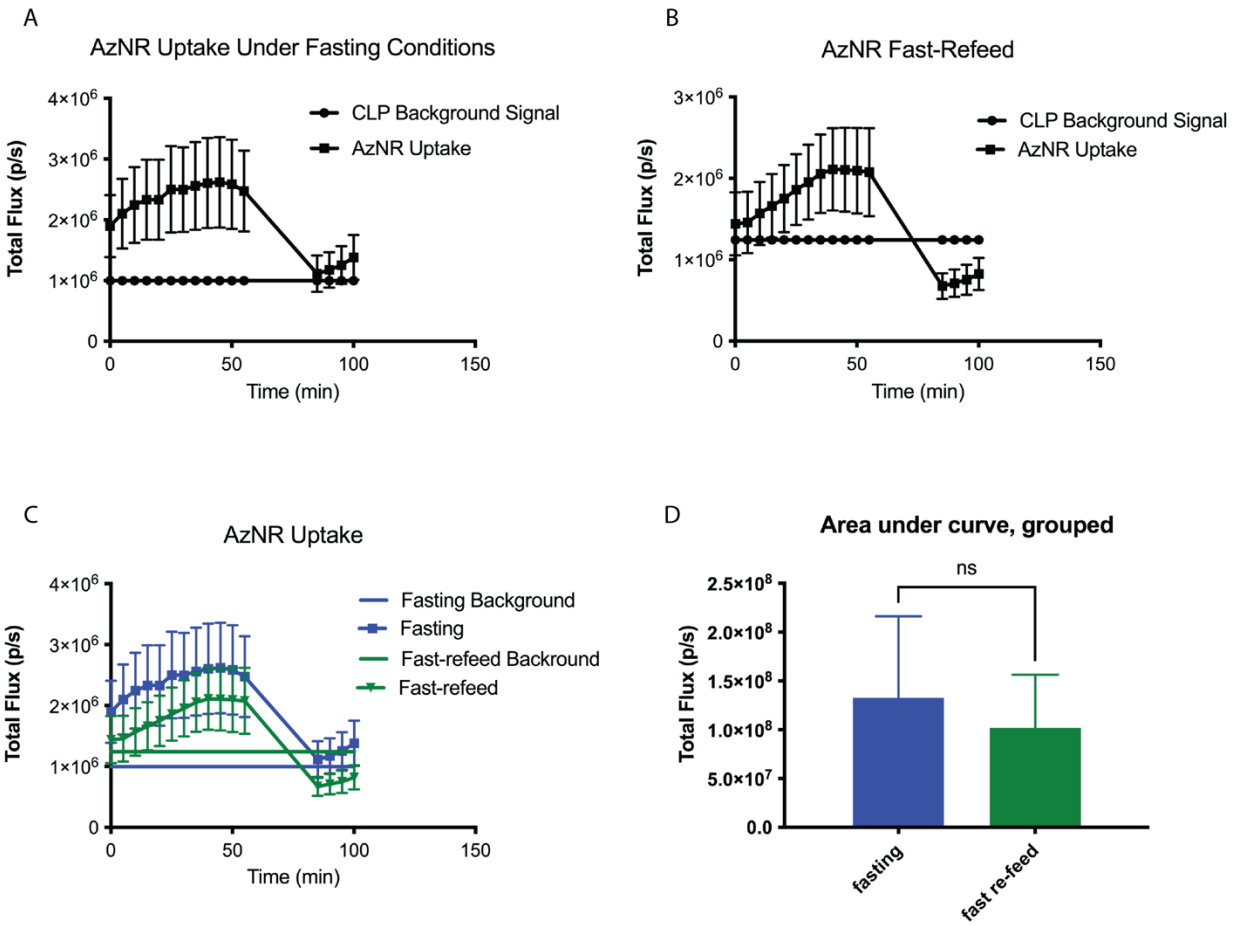

Figure 1.6. Nicotinamide Riboside Uptake

We measured the uptake of our nicotinamide riboside probe under (A) fasted and (B) fasted and then refed conditions. We (C) compared the uptake rates of the two conditions and (D) measured the area under the curve and observed no significant difference. These experiments were done in liver luciferase mice.

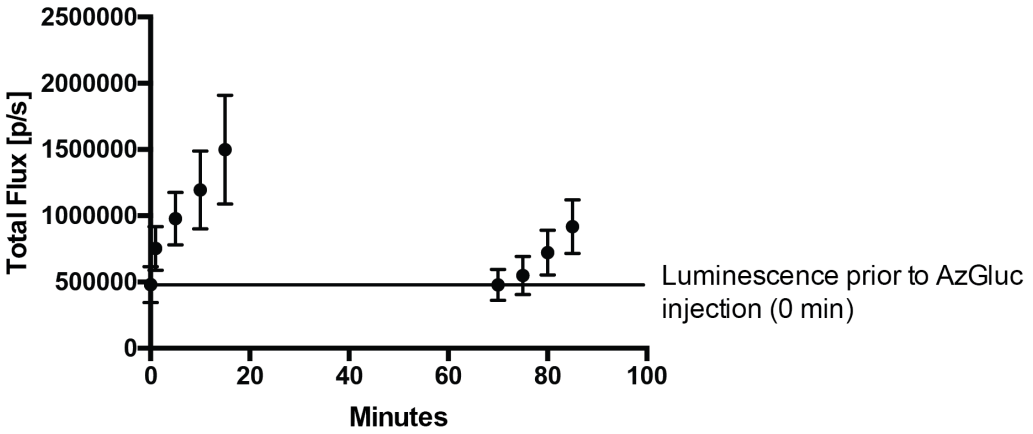

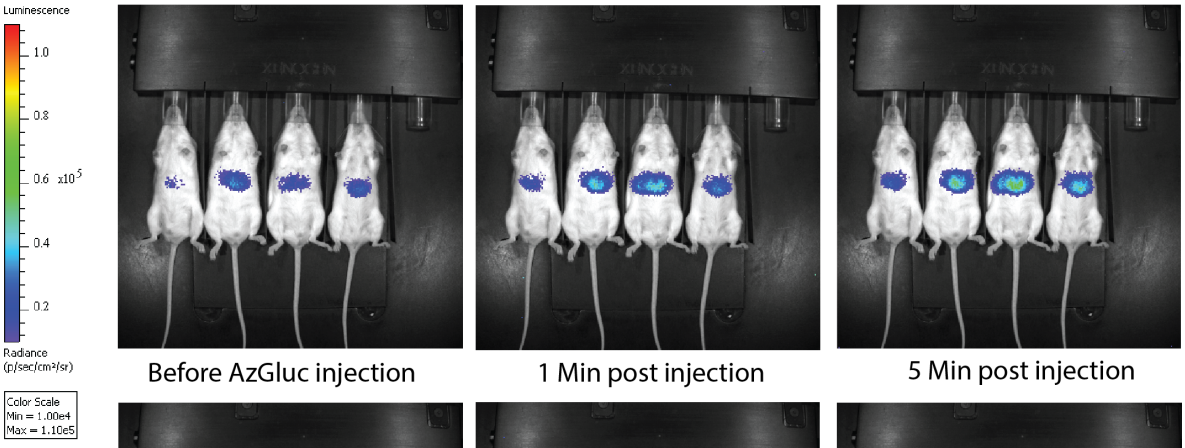

Before AzGluc injection | 1 Min post injection | 5 Min post injection

10 Min post injection | 15 Min post injection | 70 Min post injection

75 Min post injection | 80 Min post injection | 85 Min post injection

Figure 1.7 Testing bioluminescent glucose probe
In liver luciferase mice, we tested the kinetics of our glucose uptake probe by measuring uptake during the first 15 minutes after administration and for another 15 minutes at the 70-minute post injection time point to measure probe degradation. The accompanying images are included.

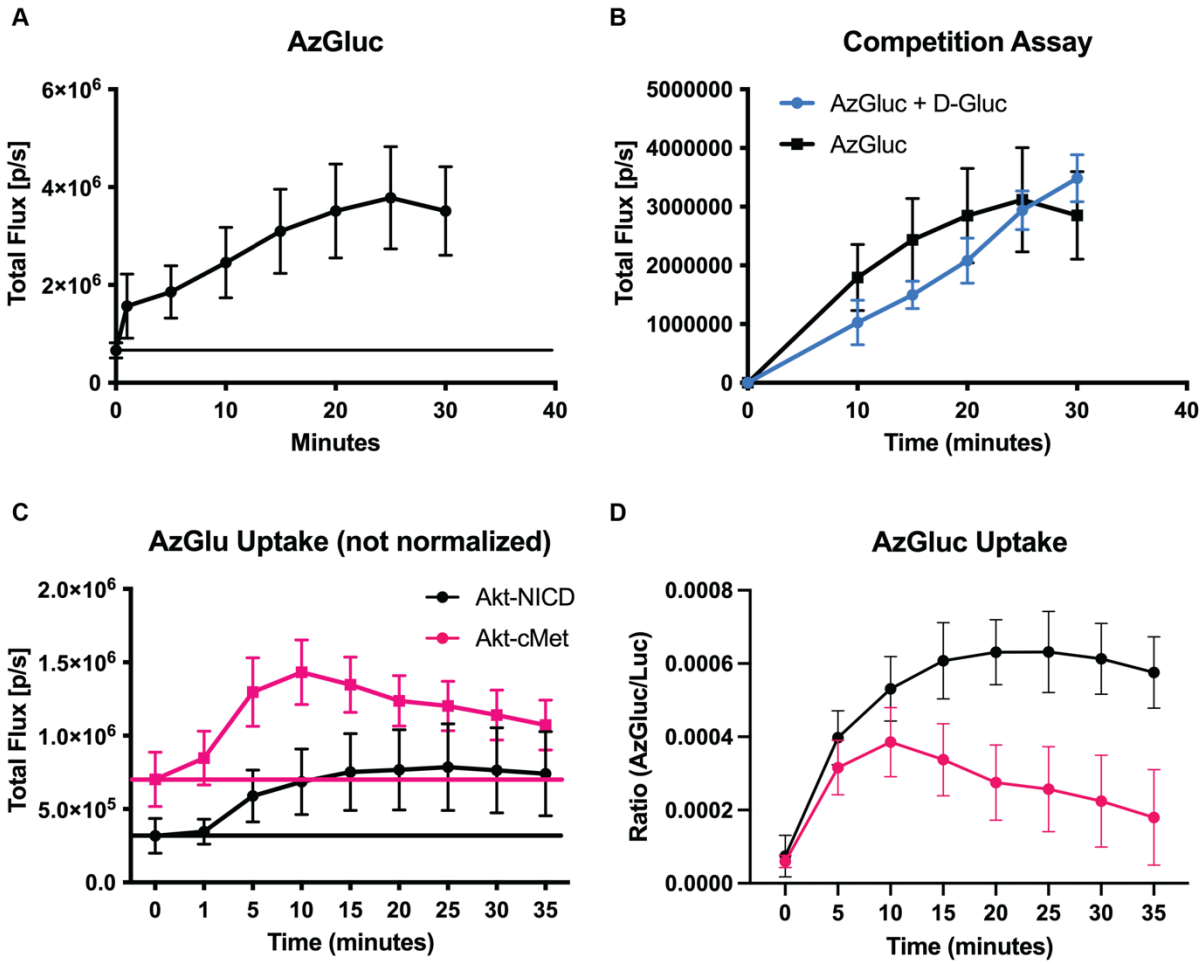

Figure 1.8. Glucose Uptake

We measured (A) glucose uptake in liver luciferase mice to establish a kinetic curve with a peak and (B) ran a competition assay to assess if the probe was being taken up in a protein mediated manner. We then tested the probe in (C) our HCC (Akt-cMet) and ICC (Akt-NICD) tumor models and (D) normalized the signal to tumor burden

A

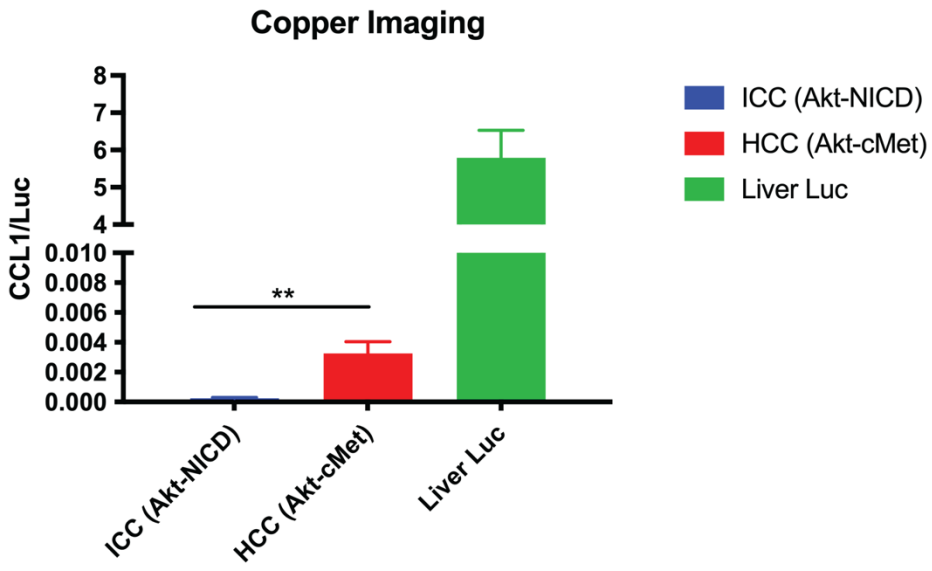

B

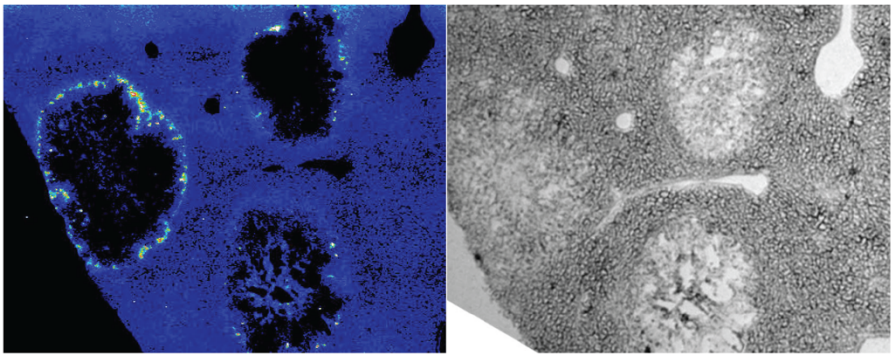

C

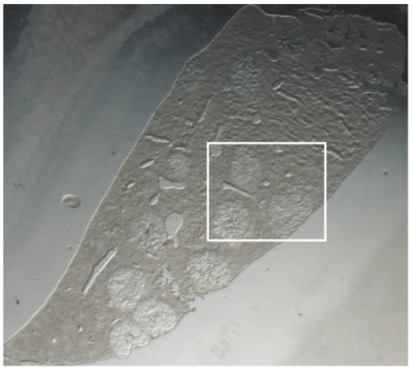

Adjacent section

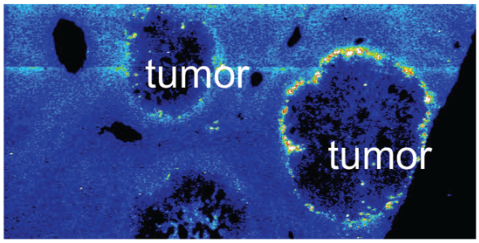

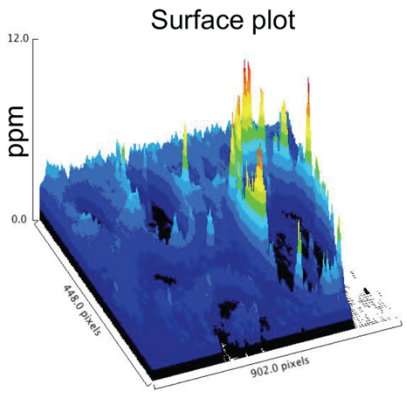

Figure 1.9. Bioluminescent copper imaging
We (A) tested out copper sensing probe in healthy liver luciferase mice and in our HCC (Akt-cMet) and ICC (Akt-NICD) mouse models where we saw a significant decrease in copper levels when comparing ICC to HCC. The low copper concentration in ICC measured with the bioluminescent probe was then (B,C) validated using LA-ICP-MS

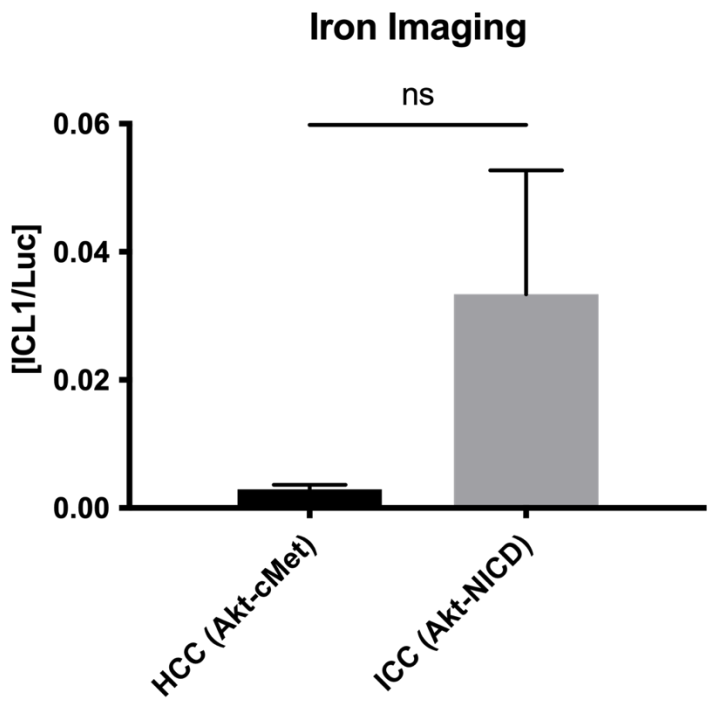

Figure 1.10. Bioluminescent iron imaging
We used a bioluminescent iron sensing probe to measure the concentration of iron in both HCC and ICC and saw no significant difference.

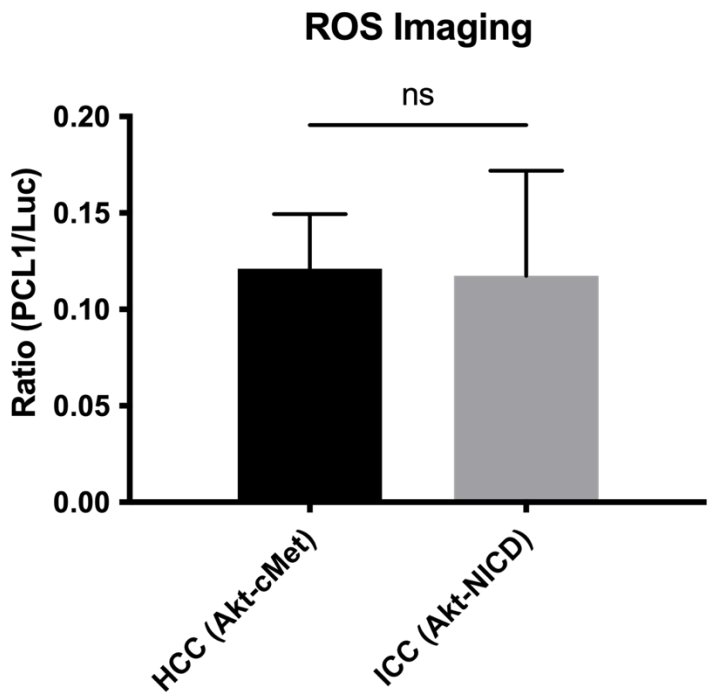

Figure 1.11. Bioluminescent hydrogen peroxide imaging
We used a bioluminescent hydrogen peroxide sensing probe to measure the concentration of reactive oxygen species (ROS) in both HCC and ICC and saw no significant difference.

Chapter 2:
Lipid Uptake and Metabolism in Intrahepatic Cholangiocarcinoma

Summary

In recent years there has been an increase in the incidence of liver cancers, specifically intrahepatic cholangiocarcinomas (ICCs), which are highly malignant adenocarcinomas of the biliary tree. Metabolic reprogramming is a common feature of cancers with many showing alterations in lipid metabolism, specifically, up regulation and dependence of de novo lipogenesis (DNL), observed through increased fatty acid synthase (FASN) activity, concomitant with a decreased dependence on exogenous fatty acids. As many tumors are reliant on FASN for growth and proliferation, the enzyme has become a popular target for new cancer treatments, but FASN dependence is not an established hallmark of cancer metabolism.

In a recent study, our collaborators demonstrated that FASN dependence is not a universal feature in liver cancers, showing that ICC development is insensitive to FASN deletion. In our study, we found that ICC maintains robust fatty acid uptake rates. Taken together, this suggests a role of exogenous fatty acids for the growth of certain cancers and ICC in particular. Importantly, cell surface proteins implicated in the uptake of fatty acids have been shown to be expressed in ICC, including but not limited to fatty acid transport proteins -2 and -5 (FATP2/5 or Slc27a2/5). Using genetic manipulation and in vivo bio-imaging techniques, we tracked the growth of ICC in an FATP5 knock out and knock down mouse models. Loss of FATP5 significantly impaired ICC growth indicating that tumor growth is dependent on exogenous fatty acid uptake. Moreover, ICC samples that grew out despite FATP5 KD, showed upregulation of FASN, suggesting that FATP5 and DNL are main points of entry for intracellular lipid pools.

We also further interrogated the lipid fingerprint of ICC when compared to our HCC model. We saw clear differences between the lipid composition of each tumor type, which is particularly interesting considering HCC relies on DNL and ICC relies on exogenous fatty acid uptake through FATP5. We saw a few classes of lipids upregulated in ICC, including some signaling lipids, structural lipids, and acyl carnitines which are implicated in energy generation. In an attempt to determine if there was a functional difference in the differential handling of lipids, we treated ICC containing mice with a CTP1 inhibitory, etomoxir, to see if beta oxidation played a significant role in fueling tumor growth.

Introduction and Background

Liver cancer is cancer is a leading cause of cancer related deaths while not being in the top ten most diagnosed form of cancer according to CDC data published in 2019 [73,74]. Its five-year survival rates are 31% for local, 11% regional, and 2% for distant stage tumors, giving liver cancer patients a poor prognosis. The two major forms of liver cancer are hepatocellular carcinoma (HCC) and intrahepatic cholangiocarcinoma (ICC), HCC being the most common and ICC making up about 10% of all liver cancer cases[74-77]. While limited targeted treatments for HCC exis[78-81]t, few treatment options exist for ICC with surgical resection being the only curative treatment although associated with a very high rate of recurrence [82,83]. These data demonstrate the necessity for more research on liver cancer mechanism and subsequent development of new treatment strategies.

Cancer metabolism is an established hallmark of cancer and research of cancer metabolism as a pathway for new treatment options is a growing field [84-88]. Cancer cells alter their metabolism and metabolic fluxes to meet the increased bioenergetic and biosynthetic demands required for cell proliferation. The Warburg effect is one of the most well-known metabolic alterations seen in cancer[36,37,89]. It is characterized by upregulation of glucose uptake and lactate production, termed aerobic glycolysis. This increase in glycolytic flux allows for a backup of intermediates to supply offshoot pathways, including those involved in macromolecule synthesis. Despite the heterogeneous and plastic nature of tumors, research has begun to uncover common pathways and behaviors involved in supporting tumor growth.

Alterations in lipid metabolism are seen in many forms of cancer and play an important role in many cellular processes including proliferation, and energy homeostasis [40,90-93] Lipids are essential molecules used for energy storage, signaling, membrane synthesis, and many other processes. One of the common upregulated pathways seen in tumors is the upregulation of de novo lipogenesis (DNL) [92-94]. Targeting DNL by inhibiting fatty acid synthase is a common anti-cancer strategy taken by many cancer metabolism researchers, developing and testing pharmacological inhibitors to prevent tumor proliferation by cutting off the main source of fatty acid acquisition [95-100]. Newer research has also uncovered a fatty acid uptake phenotype in certain cancers, identifying a secondary pathway utilized by cancers to replenish their lipid pools [101,102]. Various proteins are implicated in fatty acid uptake including CD36, fatty acid binding proteins (FABPs), and fatty acid uptake proteins (slc27a1-6). Suppressing fatty acid uptake has shown to be effective in prostate cancer [103]. This variability in lipid acquisition allows for metabolic flexibility in cancer cells, but it is still unclear how or if cells can utilize both lipid acquisition pathways, though there are some studies that show upregulation of uptake machinery upon FASN inhibition suggesting the use of only one pathway at a given time [104,105]. This study will focus on the pathways through which liver cancers utilize to replenish their lipid pools and assess if targeting lipid uptake is a viable strategy for new cancer therapeutics.

Hydrodynamic Injection

Hydrodynamic injection is a technique where you inject about 9% of body weight by volume of saline into a mouse through a tail vein injection in 5-7 seconds to allow for intracellular delivery of membrane impermeable substances in the liver. The injection works by delivering the

solution up to the heart and the high volume and high pressure allows for the backflow of the saline through the hepatic vein, pressurizing the liver and permeabilizing the hepatocytes to take up the solution [106]. Through this process the liver rapidly expands but returns to its original size in 30 minutes and the cells regain their normal morphology by 24-36 hours after injection [107]. This technique was first reported by Budker *et al* where they delivered 100 micrograms of naked DNA to the liver and showed that about 1% of the hepatocytes had been transfected [108]. Current techniques allow for 5-40% transfection efficiency. Studies have explored the mechanisms through which this injection works and found that the key factor to efficient transfection is the speed through which the injection is administered [106].

This technique has since been improved upon and applied in other ways. It has been tested on a variety of animals other than mice, including but not limited to rats [109,110], rabbits [111], chicken [112], and pig [113,114], through modifications in the route of injection to include other arteries, veins, and ducts compatible with that animals specific anatomy. Research has also been done to transfer this technology to transfect other tissues like muscle and kidney [115]. There have been many advances in this technique and results are very effective in murine systems but less so in mid to large sized animal and requires catheterization of the organ vasculature coupled with direct injection into the target organ [116]. These data show the promise of this technique as a nonviral approach to deliver nonpermeable molecules, like DNA, intracellularly to allow for gene editing[117,118], protein level modulation[119,120], gene therapy[121-123], and establishment various disease models[116].

This technique has been used to establish different liver disease models including Hepatitis B [124] and cancer[66,118], and to deliver therapeutic genes. To stably integrate the genes delivered, the hydrodynamic injection has been couples with the delivery of Sleeping Beauty transposon system [122,123,125,126]. The cancer models used in this study leverage this technology to establish HCC and ICC systems [66-70,127].

Fatty Acid Transport Proteins

The fatty acid transport proteins, also name slc27a1-6, is family of 6 proteins implicated in the uptake of long chain fatty acids. The first protein was identified in 1994[128] and the rest of the family was characterized by Hirsch et al and found to be evolutionarily conserved [129]. Each protein has a different tissue localization and has slightly different function.

Slc27a1 is found in brown and white adipose tissue, heart, skeletal muscle, skin, brain, kidney, and endothelial cells. It is implicated in long chain fatty acid transport and very long chain fatty acid activation[130]. In adipocytes and skeletal muscle, it is insulin sensitive and translocations to the membrane when stimulated. In FATP1 null mice, insulin stimulated fatty acid uptake in adipocytes is ablated and an alteration in postprandial serum long chain fatty acid regulation. This causes a redistribution in fatty acid from adipose tissue to muscle and liver leading protection from diet induced obesity and is slightly protective against insulin desensitization [131]. The protein has also been found to be over expressed in forms of melanoma and its inhibition has been shown to decrease the progression of tumor growth [132].

Slc27a2 is found in liver and kidney and is both implicated in fatty acid uptake and has shown to have acyl CoA synthetase activity [133]. It is implicated in many diseases including fatty liver disease[134], type 2 diabetes mellitus[134,135], the formation of cancer immunity[136-138], and kidney disease[135,139].

SLC27a3, 4, and 6 all also are implicated in both fatty acid uptake and have acyl CoA synthetase activity[140]. Not much is known about slc27a3 but it is localized in mouse adrenal gland, testis, ovary, and lung[141]. Slc27a4 is expressed in enterocytes and skin. It was first identified as a major intestinal fatty acid transporter and is linked to the disease restrictive dermopathy[142-146]. It has also been identified as a target for insulin signaling and has been observed to have high expression levels in clear cell renal cell carcinoma[147,148]. Slc27a6 is almost exclusively expressed in the heart where it colocalizes with CD36 and its also been seen, at lower levels, in the skin[149]. As fatp6 plays a role in fatty acid uptake in the heart, it plays a potential role in cardiovascular disease (CVD). In a study done in human, researchers were able to associate a variant of FATP6 to protective effects when looking at CVD related signifiers, like heart function and blood pressure, and diabetic phenotypes.

Slc27a5 is found exclusively in the liver and is implicated in long chain fatty acid uptake and is also a bile acid-CoA ligase [150,151]. It has been shown to play a role in both lipid and bile acid metabolism[152]. Its ablation is both protective against diet induced non-alcoholic fatty liver disease (NAFLD), decreasing hepatic fatty acid uptake and redirecting lipids to other tissues, and is able to reverse already established NAFLD In mice[153]. Low levels of FATP5 was also associated with lipid loss in the progression of NAFLD to nonalcoholic steatohepatitis, again showing FATP5's large role in hepatic lipid regulation[154]. FATP5, like other members of the transporter family, has been implicated in cancer development[155-157]. Studies have been conducted to find potential inhibitors of FATP5 for therapeutic approaches[158]. Two bile acids, ursodeoxycholic acid (UDCA) and deoxycholic acid (DCA), were found to be inhibit FATP5 and prevent the uptake of long chain fatty acids [159].

<u>*De novo* lipogenesis and Uptake</u>

The generation of fatty acids from carbohydrates intracellularly is termed *de novo* lipogenesis (DNL). Every cell has the ability to shunt excess sugars through DNL in order to make lipids which are then esterified to triglycerides and stored in lipid droplets. These lipids can later be utilized for energy production through beta-oxidation if an energetic need arises.

The process of DNL begins as a branch off the TCA cycle. Citrate is pulled out of the mitochondria via a citrate transport protein into the cytoplasm. Citrate is then converted to acetyl-CoA by ATP-citrate lyase (ACLY). Acetyl-CoA is carboxylate by acetyl-CoA carboxylase (ACC) to form malonyl-CoA. Malonyl-CoA is the initiating molecule to begin generating one palmitate molecule. Fatty acid synthase (FASN) is a multienzyme complex that adds 2 carbons donated from acetyl-CoA to malonyl-CoA in a four-step process. This process continues, with acetyl-CoA donating two carbons until a palmitate is generated[160].

Lipids necessary for cell growth and function can also be taken up from circulation. This is the primary way healthy cells acquire lipids. These lipids can either be dietary or lipids released from adipose tissue stores. Lipids in circulation take the form of either chylomicrons or VLDLs. Lipoprotein lipases in capillaries hydrolyze triglycerides from these lipoprotein particles into free fatty acids for cellular uptake. While free fatty acids can slowly diffuse across cell membranes, they are actively taken up through protein transporters, the main ones being CD36 and FATPs[161].

Results

It is widely accepted that metabolic dysregulation is a cancer hallmark, with aerobic glycolysis being a key metabolic signature. Often coupled with aerobic glycolysis is a metabolic switch from exogenous fatty acid uptake to de novo lipogenesis, commonly depicted as an offshoot of the Warburg effect. Work published by our collaborator, Xin Chen, showed in a model of intrahepatic cholangiocarcinoma (ICC) an absence of significant of de novo lipogenesis and an exogenous fatty acid uptake signature, which is contrary to most widely understood cancer metabolism [68]. To further interrogate this metabolic phenotype, we used various imaging techniques to characterize uptake rates and establish the protein target implicated in uptake.

As stated in chapter 1, we were able to establish a lipid uptake phenotype in our ICC model that was not replicated in either of our HCC models (**Fig.1.4**). While ICC showed high and physiologically significant fatty acid uptake levels contrary to HCC, the question remained if exogenous fatty acid uptake was ICC's main mode of replenishing its fatty acid pools. Using heavy water labeling, we measured de novo lipogenesis (DNL) rates by way of palmitate synthesis in triglyceride fraction in ICC and HCC at 5 weeks post injection (**Fig. 2.1a**). Both HCC models had high DNL levels when compared to non-tumorous tissue, as is expected by a model exhibiting a more traditional DNL dependent cancer metabolic phenotype. ICC on the other hand had DNL levels equivalent to nontumorous liver tissue, signifying that DNL did not significantly contribute to replenishing lipid pools in our ICC model. This suggested that ICC was relying exclusively on exogenous fatty acid uptake to fulfill its anabolic requirements.

While the modes of lipid acquisition seemed to differ between these models, it was unclear if this affected the lipid handling or levels of particular groups of lipids. We ran targeted lipidomic on ICC (Akt-NICD), HCC (Akt-Ras), and non-tumorous tissue to look at the lipid signatures in each respective cancer type to identify any metabolic difference. We normalized each lipid species to the average of the nontumorous tissue for each lipid species to obtain fold change from non-tumorous tissue to see which species were significantly up or down regulated, then created heat maps and performed a clustering analysis to visualize differences between the tumor types and non-tumorous tissue (**Fig. 2.2b**). We observed ICC and HCC to indeed have distinct lipid signatures as displayed in the clustering. All samples in each group, ICC, HCC, and non-tumorous tissues, cluster within their groups with ICC being the largest outlier. HCC is more closely related to non-tumorous tissue than it is to ICC based on this data, showing a significant difference in the lipid profile of each tumor type. We also generated a second heat map with lipid species of greatest interest and again saw similar high-level patterns (**Fig. 2.2c**).

We then looked at individual lipid classes to identify specific metabolic differences and plotted the fold change using bar graphs (**Fig. 2.3a-d**). ICC had higher free fatty acid levels than HCC which was to be expected in a model that is importing free fatty acids from circulation. ICC also had significantly higher levels of structural lipids, acyl-carnitines, and signaling lipids like ether lipids, endocannabinoids, and diacylglycerol (DAGs). This suggested ICC to not only use exogenous fatty acids as basic cellular building blocks to fuel rapid growth, but also suggested a

differential handling of lipids, shunting them preferentially into other metabolic pathways such as energy metabolism and signaling.

In order to identify through which pathway our ICC model is acquiring exogenous fatty acids, we measured expression levels of proteins known to be implicated in fatty acid uptake, including the SLC27a family of proteins also called fatty acid transport proteins (FATPs) (**Fig. 2.3a**). We found the predominant liver isoforms of the FATPS, FATP5 and FATP2, expressed in ICC at similar levels to non-tumorous liver in comparison to both HCC models which had very low levels of these transporters. Based on this data, we continued to explore the effect FATP5/2 mediated lipid uptake has on ICC (and HCC) growth.

First, we established the ICC model in whole body FATP5 knockout mice [150] and measured tumor growth over the course of 6 week (**Fig. 2.4d,e**). We saw a significant reduction in tumor growth rates in the FATP5 KO group when compared to the wild type controls. While we observed very minor growth in the FATP5 KO group, this suggested that ICC is partially dependent on FATP5 mediated uptake for growth. We hypothesized that the minor growth seen in the FATP5 KO system could either have been due to the knockout mice having compensated for the lack of FATP5 or that FATP2 also played a minor role in exogenous fatty acid uptake.

We then established an adeno-associated virus (AAV) mediated FATP5 and FATP2 knock down system (**Fig. 2.5a**). We injected 1x10^11-2x10^11 viral particles/uL of either FATP5 targeted, FATP2 targeted, or scramble control AAV one week prior to hydrodynamic injection to ensure that knock down had been established. We then proceeded to image the mice once per week to measure growth rates (**Fig. 2.5b-f**). While FATP2 knock down had a non-significant and minor effect on ICC growth, FATP5 had a strongly significant effect. We observed little to no tumor growth in the FATP5 knock down group as compared to the FATP2 and scramble control groups. We ended this experiment at 5 weeks post injection when the scramble control group reached high tumor burden.

This experiment was then repeated in both of our HCC models (**Fig. 2.5d-f**). We wanted to test if this effect was indeed related to the fatty acid uptake phenotype previously measure or because of a secondary effect of knocking out or knocking down the transporter. In our Akt-cMet model, we knocked down both FATP5 and FATP2 and in our Akt-Ras model, we knocked out only FATP5. Again, we tracked growth through weekly imaging for 5 weeks total until high tumor burden was reached. In both experiments we saw no growth inhibition effects on the tumors, further establishing that FATP5 ablation, and preventing the uptake of exogenous fatty acids, is preventing ICC tumors from growing out. The growth inhibition effects seen in ICC were not caused by a secondary effect of ablating FATP5.

While FATP5 knockdown was shown to have a strong inhibitory effect on ICC tumor growth over the course of 5 weeks, we wanted to see if the inhibitory effects were just short term or if tumors grew out given more time to adapt to the lack of FATP5. We carried out a survival experiment over the course of 32 weeks (**Fig. 2.6a,b**). We sacrificed animals when they either

reached high tumor burden determined through bioluminescent imaging or if mice started presenting signs of distress (scuffed fur, lethargy, hunched, dehydration, etc.). All SCR control and FATP2 mice were sacrificed by week 7 but 4 out of 7 FATP5 knockdown mice survived until the end of the experiment and showed little to know tumor burden (**Fig. 2.6c**). Of the 3 mice that overcame FATP5 knock down, two had upregulated FASN, suggesting that FATP5 is not only essential in exogenous fatty acid uptake but also that the only other mean of replenishing cellular lipid pools is to upregulate de novo lipogenesis (**Fig. 2.6d**). With only an n=2 presenting this ability to switch to DNL, this seems to be a rarer phenotype and would need further investigation into the regulatory mechanisms behind both DNL and exogenous fatty acid uptake pathways.

After establishing that ablating FATP5 could slow or stop tumor growth, we wanted to test if in a system where circulating lipids were higher, if that would promote tumor growth. We planned to establish a diet induced obesity model and couple it with our hydrodynamic injection. We high fat fed C57bl/6 mice for 6 weeks and then hydrodynamically injected them to establish our tumor system (**Fig. 2.7a,b**). At one week post injection, we saw little to no light signal when compared to chow fed mice. At this timepoint, fatty liver disease had developed in the mice, and we hypothesized that the changes to the liver were affecting the efficiency of the hydrodynamic injection. To troubleshoot this system, we repeated this experiment in mice that were high fat fed for only 4 weeks, before the onset of fatty liver disease (**Fig. 2.7c**). At this timepoint, we were able to image for and establish tumor nodules.

We proceeded to repeat this experiment in mice that were high fat fed for 4 weeks (**Fig. 2.7d**). We established our ICC model in both chow fed and high fat diet fed C57Bl/6 mice and imaged them for tumor burden once a week for 7 weeks. While we were able to establish significant tumor burden in our chow fed mice, we were unable to establish tumor nodules in our high fat fed mice. While we wanted to test ICC growth rates in an obesity model after establishing the necessity of exogenous fatty acids for tumor growth, our hydrodynamic transfection model was incompatible with a high fat diet obesity model in mice.

While we have been able to establish that ICC is dependent on FATP5 mediated exogenous fatty acid uptake to replenish its lipid pools and subsequently for tumor growth, the correlation between this rare lipid uptake phenotype and the poor prognosis of ICC begged the question of how these lipids were being handled upon uptake and if lipids were handled differently depending on how they were acquired, DNL or exogenous uptake.

Based on the previously mentioned lipidomics data, the most likely use for these lipids would be to shunt them into energy metabolism, specifically beta-oxidation. To test the contribution of beta oxidation to tumor growth we administered 30mg/kg/day of CPT1 inhibitor etomoxir to ICC mice through their drinking water (**Fig. 2.8a**). We started administration of the compound upon hydrodynamic injection and delivered the same dose through the end of the experiment. Throughout the experiment, we monitored water intake of both groups to ensure there was no dosage differences throughout the experiment (**Fig. 2.9a**) and we measured the metabolic rate of the mice using CLAMS to test if the dosage of etomoxir used was creating a metabolic

change. We saw a significant difference in the respiratory exchange ratio (RER) between the etomoxir treated and vehicle treated groups during their active cycle (dark) as seen in both the hour by hour chart and in the averaging of the light and dark cycle (**Fig. 2.9b,c**). This validated that the compound was indeed inhibiting beta oxidation and pushing the cells toward glucose metabolism.

The mice were imaged once per week for 5 weeks to track tumor growth, and this experiment was repeated twice to ensure the accuracy of our results (**Fig. 2.8b-d**). We observed little to no effect on growth rates suggesting that energy generation is not a primary use of these fatty acids. While we have established that lipid uptake is the sole and primary source of lipids in our ICC model, further investigation is needed to address any differential lipid handling between cancers that utilize exogenous fatty acid uptake versus *de novo* lipogenesis to replenish their lipid pools.

Discussion

It is widely accepted that metabolic reprograming is a cancer hallmark. The Warburg effect, the most widely established cancer metabolic signature, is exhibited by an increase in glucose uptake and lactic acid production in the presence of oxygen, also termed aerobic glycolysis. Often coupled with aerobic glycolysis is a metabolic switch from exogenous fatty acid uptake to de novo lipogenesis, commonly depicted as an offshoot of the Warburg effect. In our work we show that the switch to *de novo* lipogenesis is in fact not seen in all cancers. Specifically, in our model of intrahepatic cholangiocarcinoma (ICC) we have observed an absence of significant *de novo* lipogenesis and an ability to maintain exogenous fatty acid uptake levels, which is contrary to most widely understood cancer metabolism. This presents us with a potentially new metabolic targeting strategy for liver cancer.

In this study we looked at three cancer models, HCC (Akt/Ras), HCC (Akt/cMet), and ICC (Akt/NICD), that showed differential lipid uptake phenotypes. All models have been previously characterized [66,67,69,70] and the role of de novo lipogenesis in tumor growth has been investigated [68]. HCC exhibited upregulation of FASN and a reliance on DNL for growth, while ICC showed no upregulation of FASN and no growth effect upon FASN ablation. We further validated this phenotype by measuring DNL levels using deuterium labeled water administration (**Fig. 2.1a**). Our results indicate that our Akt-NICD driven ICC model, which was previously shown to take up exogenous fatty acids, showed no increase in DNL rates when compared to non-tumorous liver control. The HCC model, which does not exhibit a fatty acid uptake phenotype, showed a significant increase in DNL rates.

FASN expression levels were also corroborated in human ICC, showing translational relevance [68]. These data suggested that while HCC relies primarily on DNL for lipid production, ICC does not and is utilizing another pathway to acquire lipid for growth and other cellular functions. Furthermore, data support our hypothesis that our liver cancer models exhibit *either* DNL or exogenous fatty acid update to replenish their lipid pools

In the previous chapter, we characterized these models looking at each tumor's ability to replenish their lipid pools through exogenous fatty acid uptake pathways. Using a bioluminescent fatty acid probe, we measured exogenous fatty acid uptake rates *in vivo* and saw that while HCC does not take up significant levels of free fatty acid, ICC does (**Fig. 1.4**). Contrary to what is typically observed in cancer lipid metabolism, this clearly illustrated an ability for tumors to utilize an alternate pathway, exogenous fatty acid uptake, to replenish their lipid pools.

Looking beyond just the modes of lipid acquisition in our two liver cancer models, we wanted to explore if there was a functional difference in the lipid handling post uptake between our models. In the clinic, ICC exhibits higher malignancy, and we hypothesized that this might be due to a differential handling and metabolism of lipids. We ran targeted lipidomics using LC-MS-MS to look at the lipid profiles of both ICC and HCC compared to nontumorous liver tissue (**Fig. 2.2, 2,3**). There was a clear difference in the lipid fingerprint of each tumor model, illustrating

that the lipids in each system are being handled and metabolized differently. A total of 95 out of 139 lipids species measured showed significant p value (< 0.05) for either ICC, HCC, or both when compared to nontumorous tissue, of which 58 lipid species showed significant differences between the two liver cancer models. This showed a clear difference in the lipid profile of each tumor type, and further illustrated the importance and relevance of characterizing the different lipid acquisition and uptake mechanisms.

To establish how these lipids were being taken up, we looked at expression levels of proteins implicated in fatty acid uptake and saw that ICC maintained relevant levels of slc27a5 and slc27a2, also known as FATP5 and 2 (**Fig. 2.4a**). These transporters have been previously implicated in hepatic lipid metabolism and other disease states including NAFLD emphasizing their utility as a metabolic target. FATP5 is also liver specific, making it an excellent target for future pharmaceutical development.

We established our ICC model in FATP5 knock out mice to explore the effect FATP5 has on tumor growth (**Fig. 2.4d**). When compared to wildtype mice, we see a significantly slower tumor growth rate in the FATP5KO mice, and by week 6/7 when we should reach high tumor burden, we see significantly lower tumor burden in the knockout mice. This shows that FATP5 ablation is impairing tumor growth and supporting our hypothesis that ICC is using FATP5 to uptake exogenous fatty acids. One limitation of this study was the use of a whole-body knockout mouse and the subsequent compensation in lipid metabolism and exogenous fatty acid uptake that may occur. Particularly considering non-tumorous liver tissue primarily relies on fatty acid uptake as a lipid source. We also did not have access to an FATP2 KO mouse to measure any functional effect FATP2 has ICC growth. To address this, we established an Adeno-associated virus (AAV) mediated knock down system to further explore the role of both FATP5 and FATP2 in ICC growth (**Fig. 2.5a)**.

We used an shRNA based AAV to knock down FATP2 and FATP5 respectively (**Fig. 2.5**). We then induced our ICC system and monitored tumor growth over time. We again saw drastic impairment of ICC growth in the FATP5 KD group, but little effect in the FATP2 KD group when compared to the scramble control. This suggests that FATP5 is the primary transporter used to import fatty acids into the cell. We also tested the effect of FATP5 KD in our HCC model to see if knockdown had any potential secondary effects that would impair growth in a tumor that does not rely on exogenous fatty acid uptake, and no growth effect was observed.

Once we established FATP5 as the primary transporter responsible for lipid uptake, we wanted to explore how long the impairment on tumor growth lasted, and if there were any compensatory mechanisms that could be utilized to replenish the cell's lipid pools. We ran a survival study using the same knockdown system and allowed the tumors to grow until 32 weeks post injections (**Fig.2.6**). Our end points for euthanasia were either reaching full tumor burden, as measured through bioluminescent imaging, or if the mouse showed any severe signs of distress as outlined by IACUC. All the mice in the scramble (n=6) and FATP2 KD (n=7) groups had to be euthanized by 7 weeks post injection. In contrast, out of 7 FATP5 KD mice, 4 exhibited

little to no tumor growth by week 32 with the other 3 being euthanized at weeks 11 and 15. This showed a strong growth defect in the FATP5 KD groups that was sustained long term.

To look for potential compensatory mechanisms in the 3 tumor grow-outs, we assayed for expression levels of FASN and observed that 2 out of 3 samples upregulated FASN to overcome the selective pressure imposed by FATP5 KD (**Fig. 2.6d**). This suggests two primary pathways for lipid acquisition, DNL and FATP5 mediated fatty acid uptake, and shows a potential for dual inhibitory therapeutic strategies to treat ICC. While the sample size for this experiment is small, the potential for future cancer treatment research is promising, particularly if exogenous fatty acid uptake is upregulated in response to FASN inhibition.

Following up on our lipidomics data, we looked for other pathways downstream of lipid uptake that could be of potential interest when developing treatment strategies. Within the group of significantly altered lipid species, we observed that ICC had higher levels of lipids implicated in growth, signaling, and energy metabolism (**Fig. 2.3**). While we were unable to follow up on the effect of signaling lipids (ether lipids, endocannabinoids, and diacylglycerol) due to a lack of inhibitors suitable for long term administration in mice, we were able to follow up on the differences in lipids implicated in energy metabolism. We observed an increase in acyl-carnitines in ICC suggesting higher fatty acid oxidation rates. Etomoxir, a CPT1 inhibitor, was administered to ICC tumor bearing mice to assess if fatty acid oxidation played a significant role in tumor growth (**Fig. 2.8**). While we saw no significant growth difference upon CPT1 administration, the lipidomics data suggests that lipids taken up exogenously are shunted into different pathways than lipids acquired through DNL and inhibiting only one of these pathways might not be enough to elicit a strong growth effect.

While it is clear we need more *in vivo* experimental tools to further explore lipid metabolic dynamics, our data clearly establishes exogenous fatty acid uptake as a main pathway for tumor lipid pool replenishment with FATP5 as an essential mediator that can be targeted to inhibit the growth of intrahepatic cholangiocarcinoma. Similar fatty acid uptake phenotypes are seen in other forms of cancer including prostate, ovarian, and breast cancers with CD36 as one of the primary mediators [103,162-164]. Targeting of uptake has shown to elicit various degrees of growth inhibition in other cancer types[165-167], bolstering our study's findings. Another group has characterized a similar fatty acid uptake phenotype in ICC [155], but were not able to identify a protein target or uptake pathway. Our group's identification of FATP5 as the essential mediator of fatty acid uptake in ICC is significant not only because of the robust growth effect shown in our study, but also because the transporter is liver specific, druggable, and non-lethal in knockout models [140,159] making it a promising new therapeutic target.

Figures

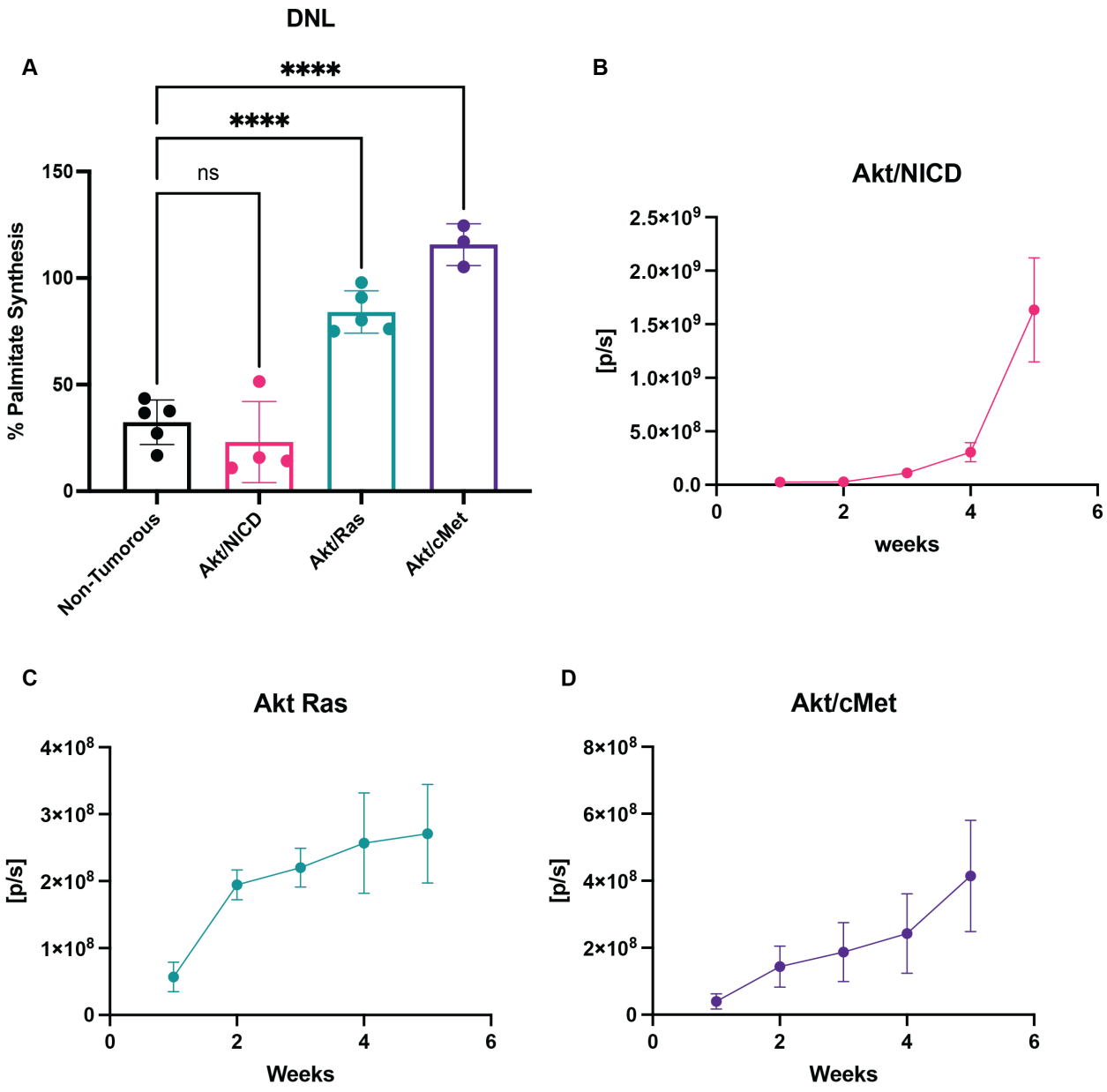

Figure 2.1. De novo lipogenesis measurements
We (A) measured *de novo* lipogenesis (DNL) rates using heavy water labeling and mass spectrometry technology in late-stage tumors. We observed an upregulation of DNL in our HCC models (Akt/Ras and Akt/cMet) when compared to nontumorous tissue but no change between ICC and nontumorous liver. We've included the growth rates of the (B) ICC, (C) HCC, Akt-Ras, and (D) HCC, Akt-cMet mouse models used in the study

A

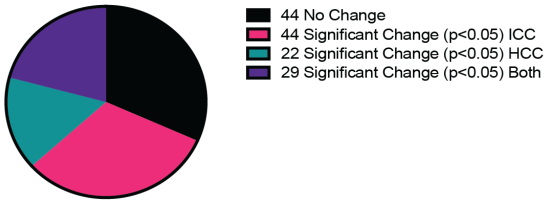
Lipid Species
44 No Change
44 Significant Change (p<0.05) ICC
22 Significant Change (p<0.05) HCC
29 Significant Change (p<0.05) Both

B

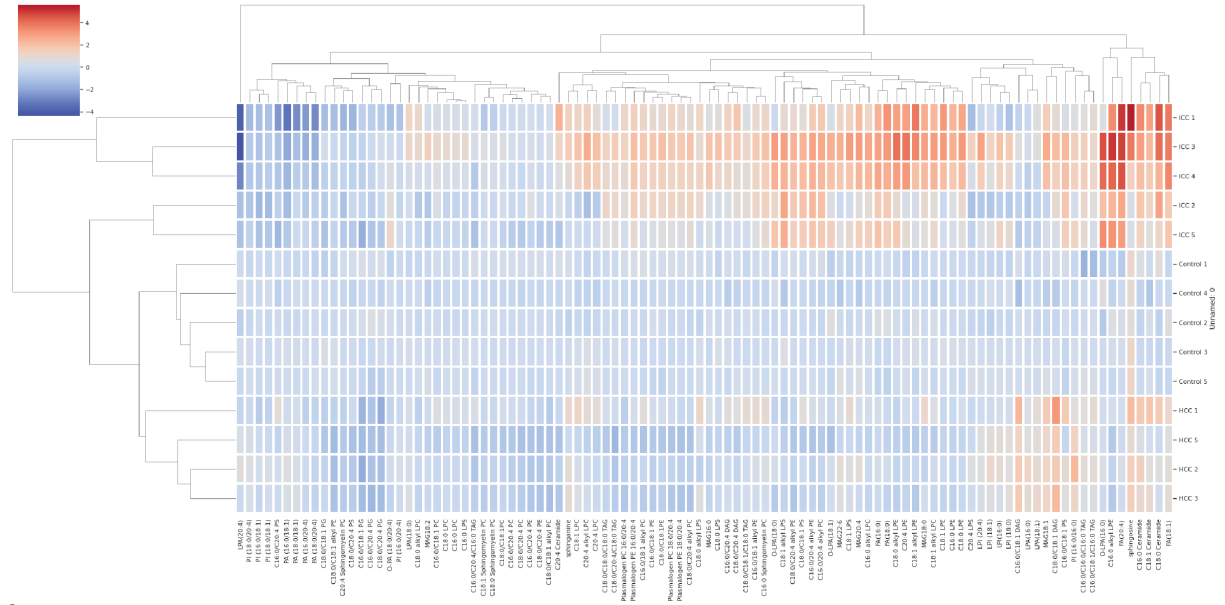
Total=139
ICC 1
ICC 3
ICC 4
ICC 2
ICC 5
Control 1
Control 4
Control 2
Control 3
Control 5
HCC 1
HCC 5
HCC 2
HCC 3
Unnamed: 0

C

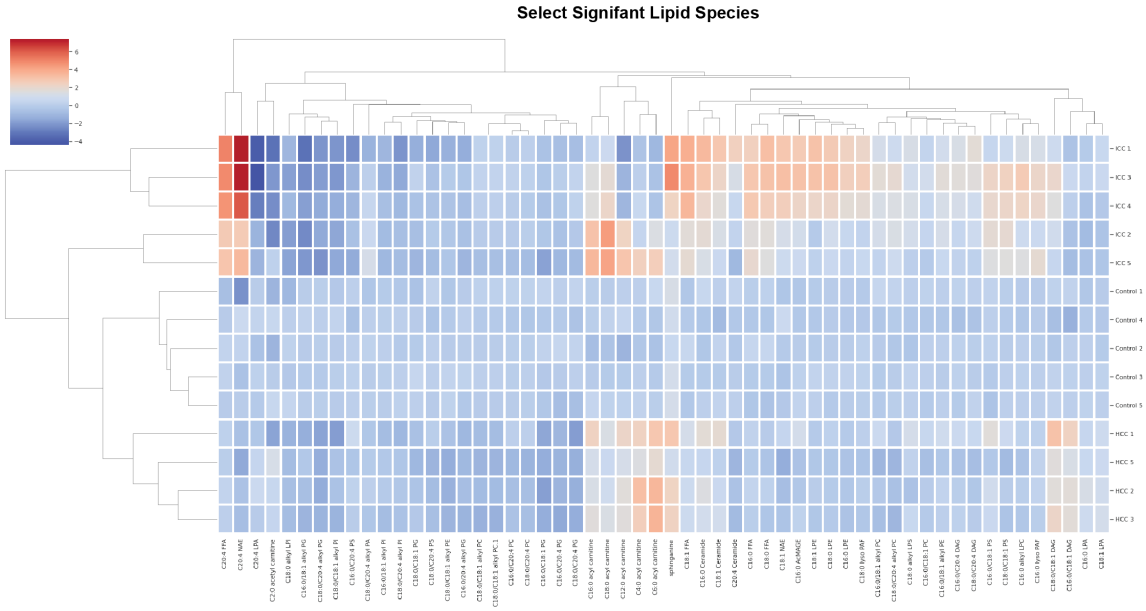
Select Signifant Lipid Species
ICC 1
ICC 3
ICC 4
ICC 2
ICC 5
Control 1
Control 4
Control 2
Control 3
Control 5
HCC 1
HCC 5
HCC 2
HCC 3

Figure 2.2. Lipidomics
We performed targeted lipidomics on nontumorous liver, HCC (Akt-Ras), and ICC. When compared to nontumorous tissue, (A) out of 139 lipids measured, 44 showed no change, 44 showed a significant change in ICC only, 22 showed a significant change in HCC only, and 29 showed a significant change in both tumor types. We (B) generated heatmaps and performed a clustering analysis with the data. We observed a significant difference in the lipid patterning of each group, as observed through the clustering. (C) We then generated a heatmap containing lipids of metabolic interest that showed significant differences.

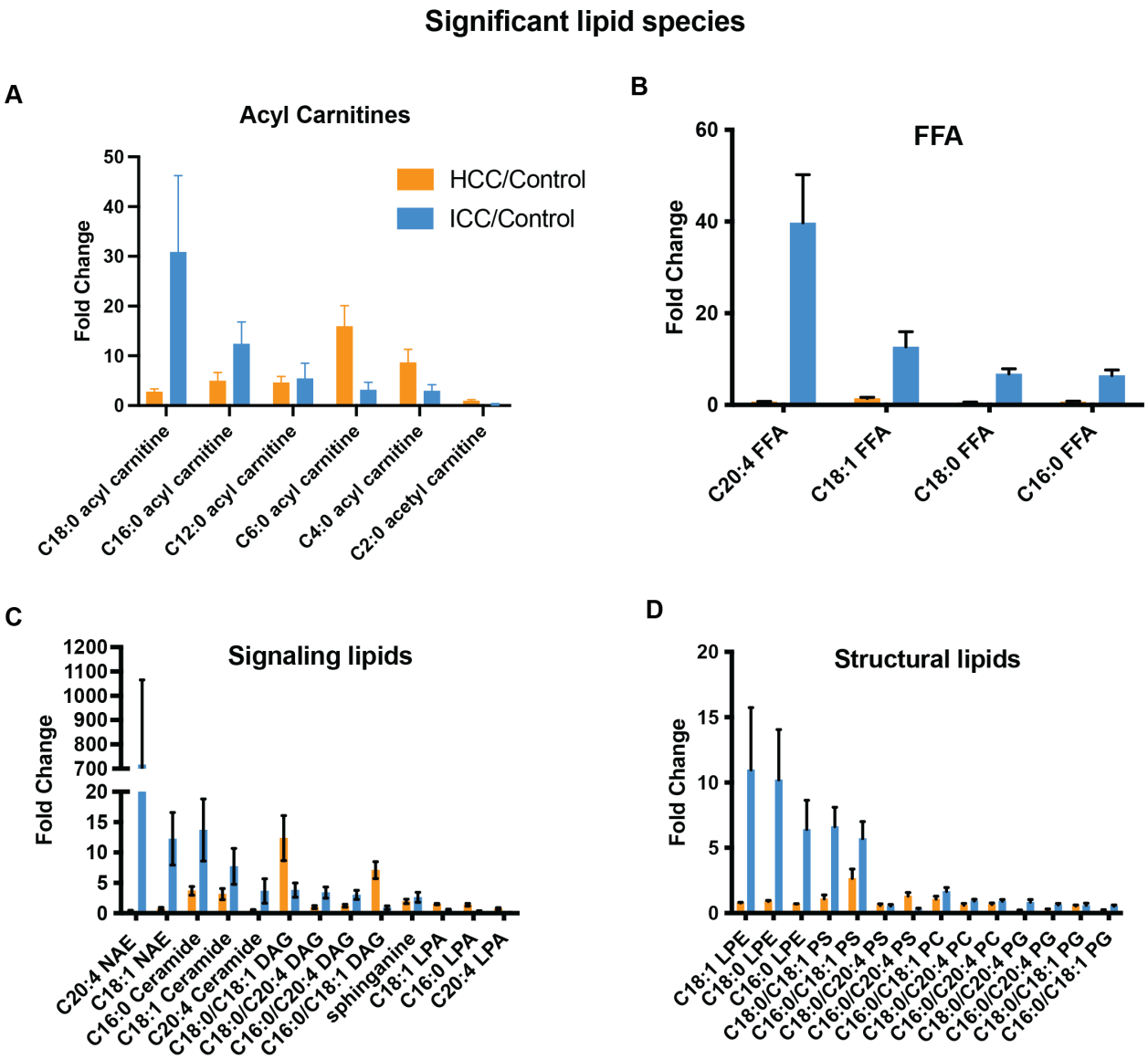

Figure 2.3. Lipidomics

Using our lipidomics data, we compared ICC and HCC after normalizing to nontumorous tissue to generate fold change. We saw (A) an upregulation of long chain acyl carnitines in ICC, (B) an increase in free fatty acids in ICC, (C) an upregulation in signaling lipids in ICC, and (D) an increase in structural lipids in ICC.

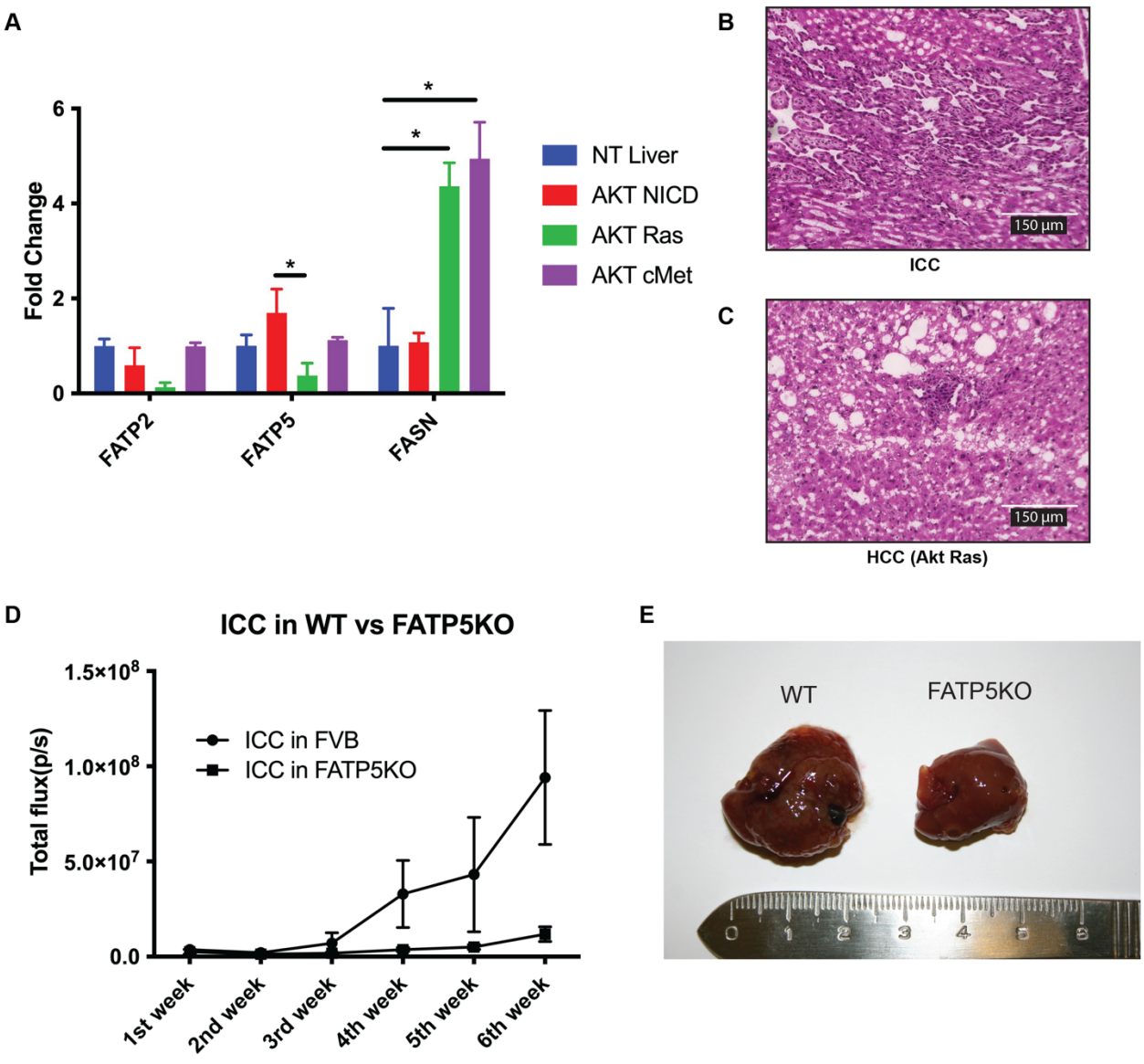

Figure 2.4. FATP5 expression levels in liver cancer and impact on ICC growth
(A) Using quantitative PCR, we measured significantly high levels of FATP5 in ICC and upregulated levels of FASN in both HCC models. We performed H&E staining of (B) ICC and (C) HCC (Akt-Ras to look at cellular morphology. To investigate the role of FATP5 in ICC growth, we established our tumor model in FATP5 knockout mice and saw a significant decrease in tumor growth as shown by (D) the growth curves and (E) photos of the ex vivo livers.

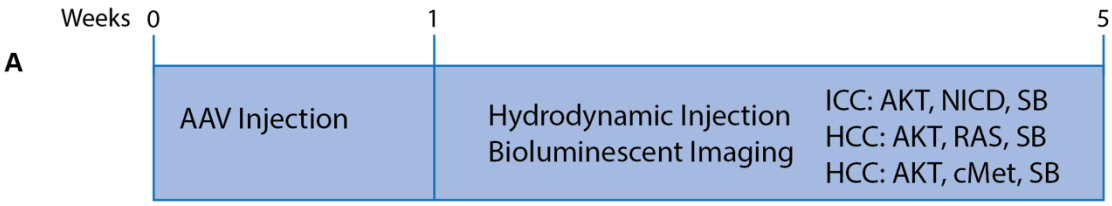
A
Weeks 0
1
5
AAV Injection
Hydrodynamic Injection
Bioluminescent Imaging
ICC: AKT, NICD, SB
HCC: AKT, RAS, SB
HCC: AKT, cMet, SB

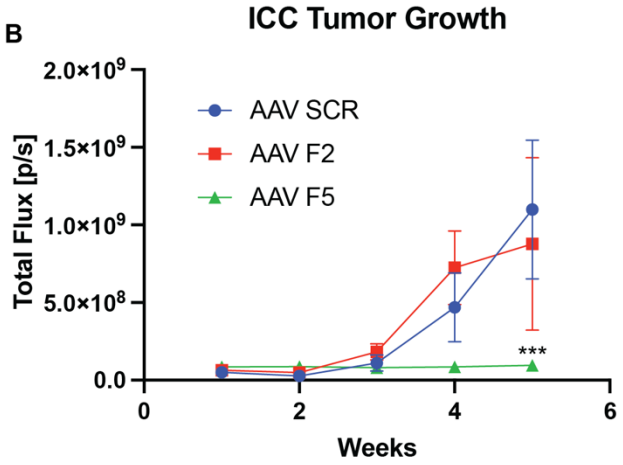
B
ICC Tumor Growth
Total Flux [p/s]
2.0×10^9
1.5×10^9
1.0×10^9
5.0×10^8
0.0
AAV SCR
AAV F2
AAV F5
***
0
2
4
6
Weeks

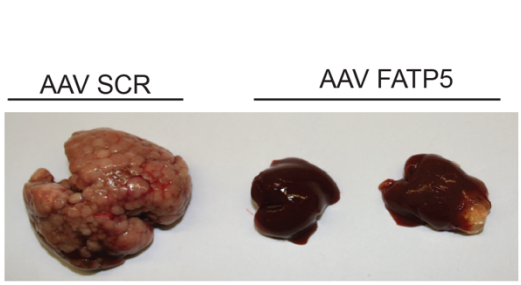
C
AAV SCR
AAV FATP5

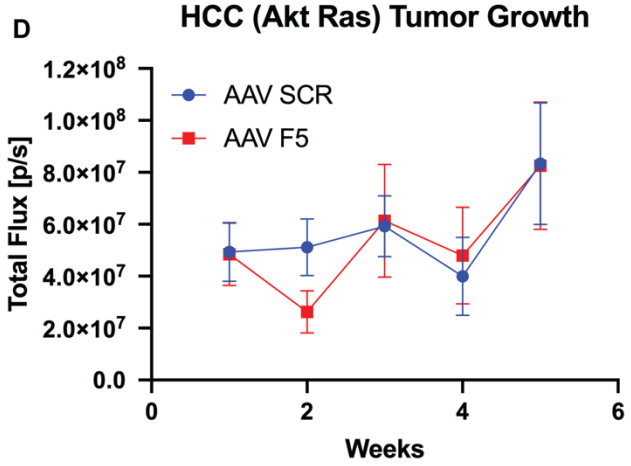
D
HCC (Akt Ras) Tumor Growth
Total Flux [p/s]
1.2×10^8
1.0×10^8
8.0×10^7
6.0×10^7
4.0×10^7
2.0×10^7
0.0
AAV SCR
AAV F5
0
2
4
6
Weeks

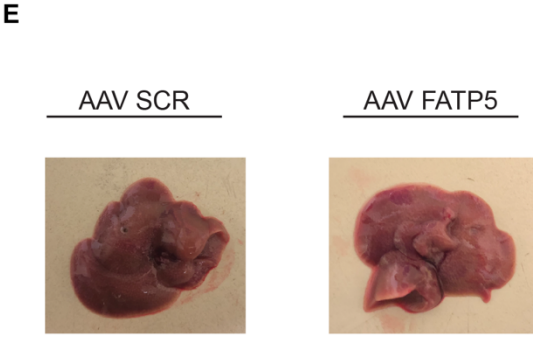
E
AAV SCR
AAV FATP5

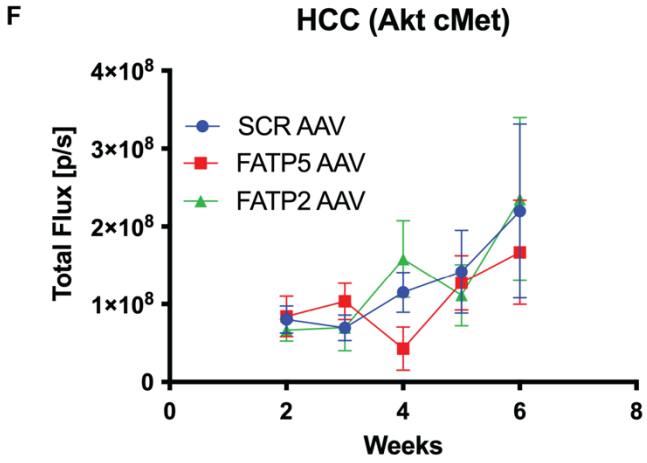
F
HCC (Akt cMet)
Total Flux [p/s]
4×10^8
3×10^8
2×10^8
1×10^8
0
SCR AAV
FATP5 AAV
FATP2 AAV
0
2
4
6
8
Weeks

Figure 2.5. FATP2/5 knockdown
Using adeno associated virus (AAV) we (A) established a knockdown system to test the effect of FATP2/5 on tumor growth in both ICC and HCC. (B,C) We saw a significant hindrance in ICC growth upon FATP5 but not FATP2 knockdown. (D-F) Knockdown of FATP2 or FATP5 had no effect on either of our HCC tumor models .

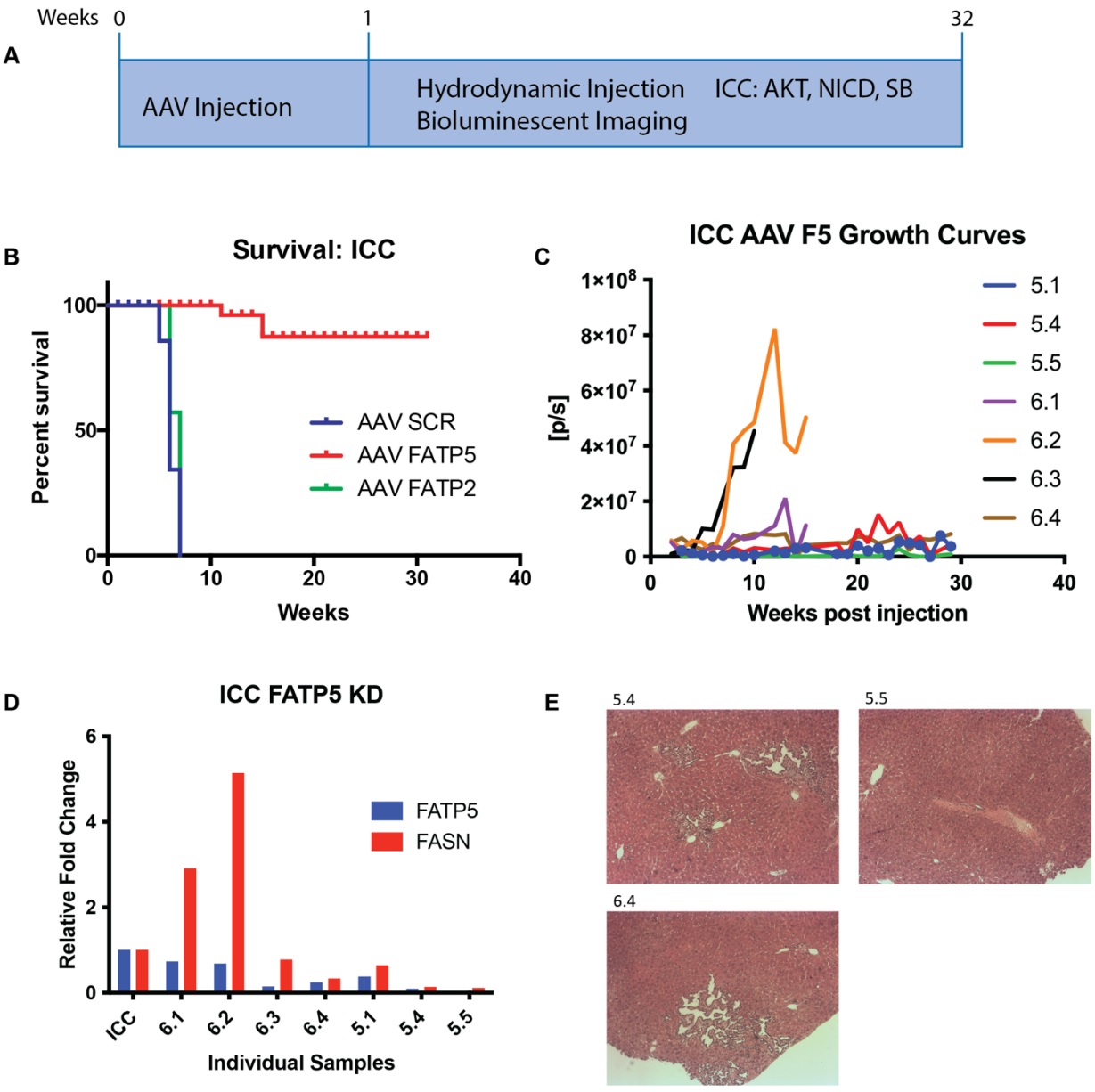

Figure 2.6. Survival Curve

We (A) established our AAV base knockdown system in ICC induced mice and (B) performed a survival experiment where we let the tumors grow until 32 weeks post injection. Mice were euthanized when tumor burden has grown to significant levels. Out of all the mice in the experiment 4 out of 7 FATP5 knockdown mice did not grow significant tumor burden. The growth curves of the FATP5 knockdown mice are displayed in (C). (D) These mice were then assayed for both FATP5 and FASN expression levels using qPCR and saw an upregulation of FASN in two of the three mice that were euthanized because of high tumor burden. (E) We performed H&E staining of liver sections taken from mice that survived until the end of the experiment. We saw normal liver histology and the establishment of small tumor nodules that did not grow over the course of 32 weeks.

A

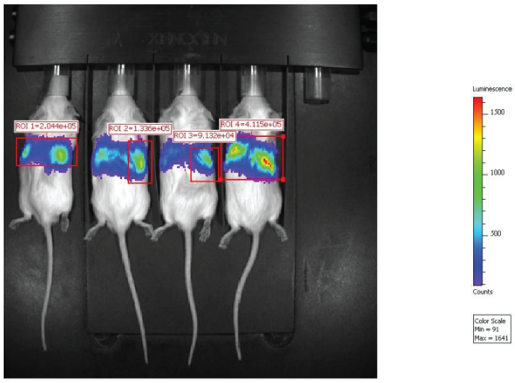

Chow Fed

B

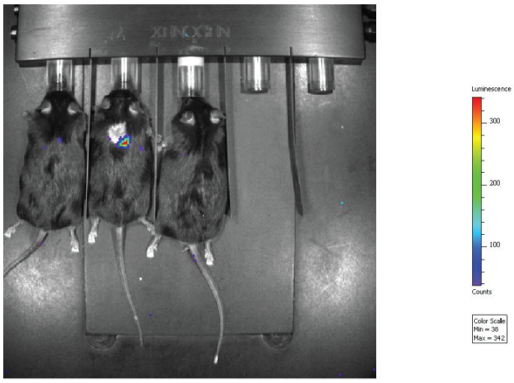

HFD 6 Weeks

C

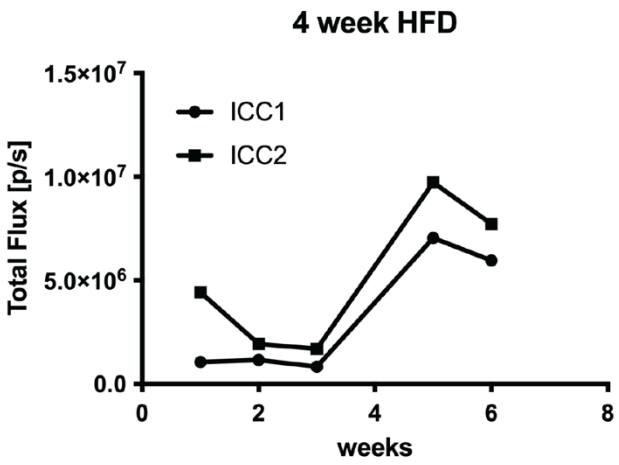

D

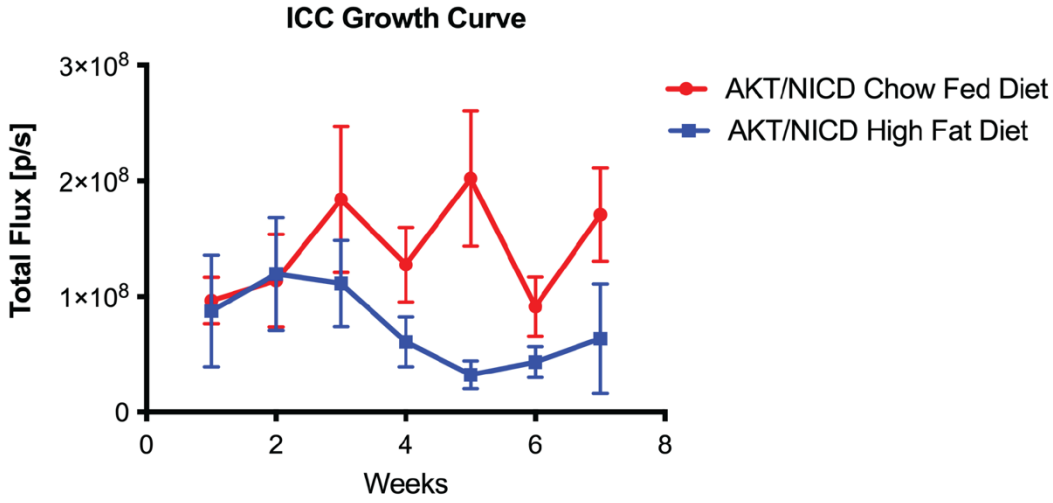

Figure 2.7. High fat diet feeding in ICC
With ICC's fatty acid uptake phenotype, we wanted to assess tumor growth in an obesity system. We tested the compatibility of the hydrodynamic injection with high fat diet fed mice. (A) Chow fed mice showed significant bioluminescent signal one week post injection but (B) mice that were high fat diet fed for 6 weeks prior to injection showed no bioluminescent signal. We re-tested our tumor system in (C) mice that were high fat diet fed for four weeks and we were able to observe bioluminescent a bioluminescent signal. (D) We ran the experiment comparing ICC growth rates in four week high fat diet fed and chow fed mice. We were unable to establish the tumor system in an obesity system.

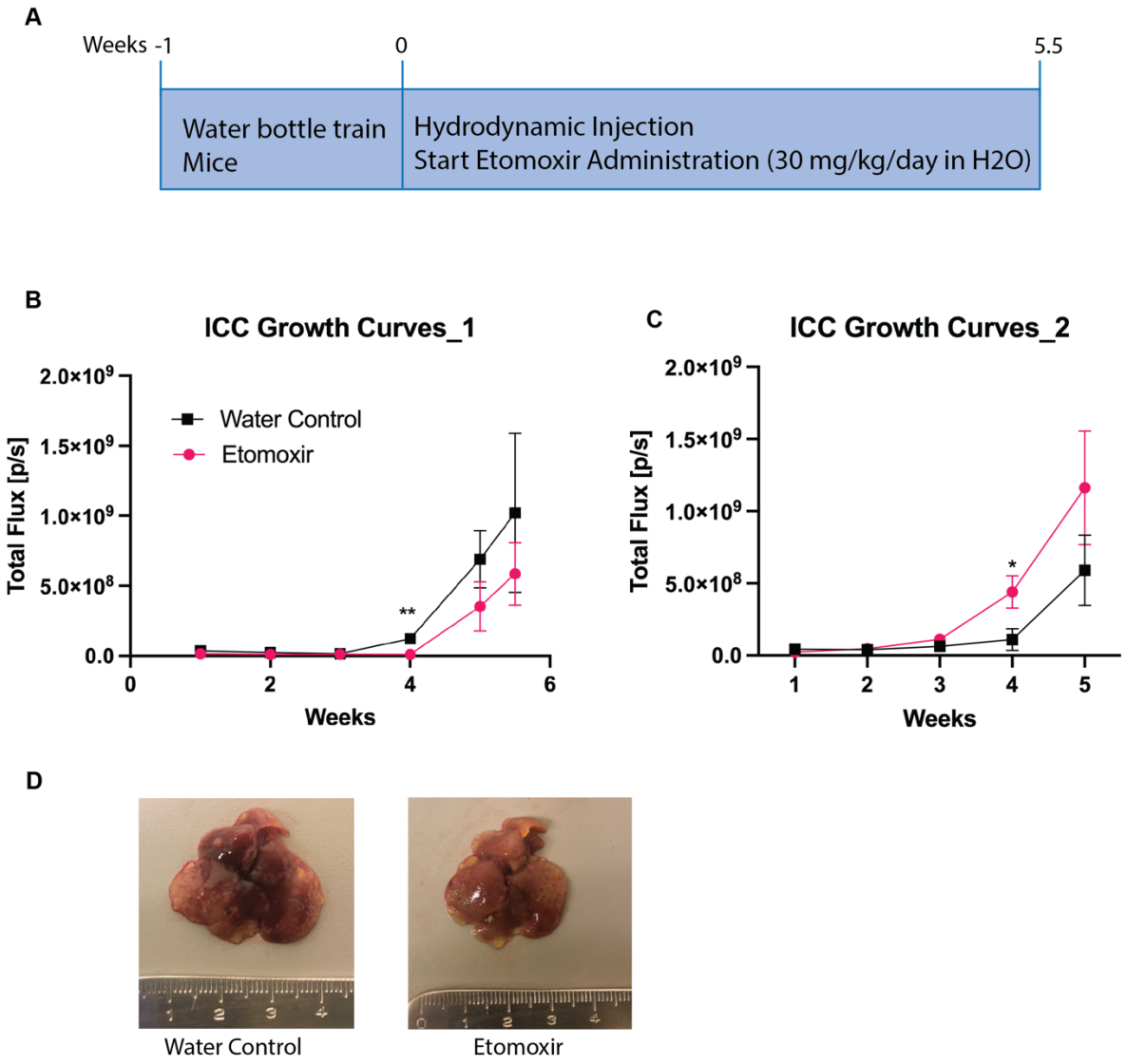

Figure 2.8. CPT1 inhibition in ICC

We (A) treated mice with etomoxir, a CPT1 inhibitor, to assess the impact of beta oxidation on tumor growth. (B-C) We ran this experiment two times, tracking tumor growth over the course of 5 week. We saw no significant difference in tumor growth as seen in the growth curves and (D) ex vivo images of the livers.

A

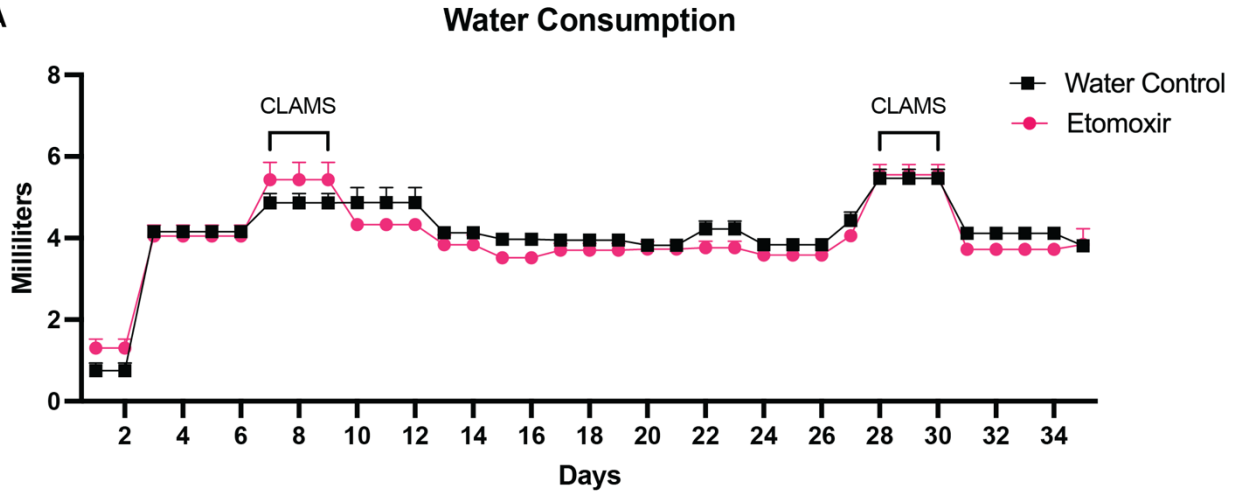

B

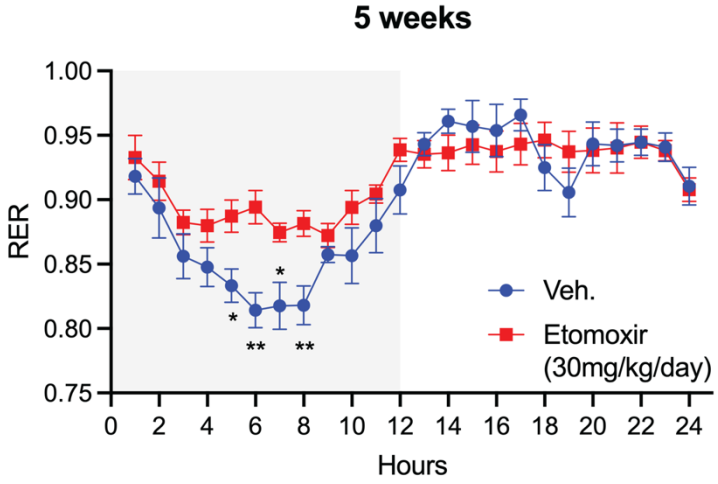

* = p-value ≤ 0.05, ** = p-value ≤ 0.01

C

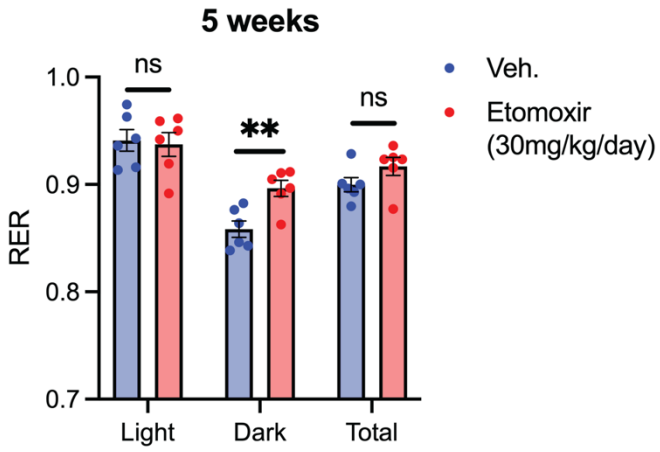

* = p-value ≤ 0.05, ** = p-value ≤ 0.01

Figure 2.9. Etomoxir validation
To validate that etomoxir was not having a secondary effect and was being administered at a consistent dose throughout the experiment, (A) we measured water intake of the mice. Both groups drank the same amount of water at a consistent rate throughout the experiment showing that the etomoxir in the drinking water did not water intake. We also measured the respiratory rate of the mice using CLAMS to make sure the dose of etomoxir was having a metabolic effect. (B,C) We saw an increase in the respiratory exchange ratio during the active phase of the etomoxir treated mice, suggesting a shift away toward glucose metabolism and from lipid metabolism, validating that the etomoxir dosage was eliciting a metabolic effect.

Materials and Methods

Animal Models

Animal experiments were approved by The UC Berkeley Animal Care and Use Committee. FVBNJ and B6(Cg)-Tyrc-2J/J (B6-Albino) mice (males aged 4-6 weeks old) were purchased from Jackson Labratory. FATP5 KO mice were obtained from our in-house colonies. Liver luciferase mice were derived by crossing stop floxed luciferase mice (FVB. 129S6(B6)Gt(ROSA)26Sortm1 (Luc)Kael/J, Strain #005125) and albumin cre mice (B6.Cg-Speer6-ps1Tg(Alb-cre)21Mgn/J, Strain #003574) as previously published[168] and the subsequent colonies were maintained in house. Mice were kept in a housing room with a 12 hour dark/12 hour light cycle and given free access to food and water.

In mouse tumor models, maximal tumor size was assessed via bioluminescent imaging. Maximal tumor size for all experiments was set at 1x10x9 p/s with other endpoint considerations including but not limited to the following conditions: tumors that interfere with normal activity; weight loss greater than 10% of baseline weight; body condition score of two or less (five point scale); clinical signs of illness such as hunched posture, respiratory difficulties, or reticence to move. Maximal tumor size in ICC survival experiment was set at 1x10^8 p/s, and mice were euthanized before this end point if the aforementioned health considerations were observed.

Hydrodynamic injection

Dilute 15ug of each oncogene containing plasmid and sleeping beauty transposase plasmid in a ration of 1:25 in 2ml of 0.9% NaCl (pharmaceutical grade), filtered using a 0.22um filter, and injected into the lateral tail vein of 6-7 week-old mice in 5-7 seconds through a 27 gauge needle. Mice were monitored closely the following 24 hours. To induce ICC we deliver pT3-EF1α-AKT-HA-IRES-Luc, pT3-EF1α-NCID1 and to induce ICC we deliver pT3-EF1α-AKT-HA-IRES-Luc and pT3-EF1α-N-RAS plasmids along with hyperactive sleeping beauty transposase (pCMV-SB) for stable integration. All plasmids were provided by our collaborator (Department of Bioengineering and Therapeutic Sciences, UCSF). Plasmids were all prepared using ZymoPURE II maxi prep (D4202), tested for purity, and stored at -20˚C.

Bioluminescent imaging

The IVIS system is utilized for all bioluminescent imaging. For each imaging session, animals are anesthetized using isoflurane/oxygen in an induction chamber prior to injection with any imaging probes. Once injected, animals are placed into the chamber of the IVIS and are maintained under isoflurane for the duration of the imaging session. Total flux (photons/second) at the maximal point of light emission (dependent on imaging probe used) is measured using the Perkin Elmer living image software.

To image tumor burden, 100ul of sterile filtered 2mM D-luciferin sodium salt (R&D systems 5427) in PBS is i.p. injected into each anaesthetized mouse immediately before imaging. The mice are imaged in 5 minute increments for a total of 15 min, with a peak signal at 10 minutes post injection.

Fatty Acid Uptake Imaging

To image fatty acid uptake, mice are i.p. injected with 100ul of 200 uM FFA-Luc in 0.1% (wt/vol) bovine serum albumin–containing phosphate-buffered saline (0.014 mg/mouse). Fatty acid probes are stored in 20mM (100x) stocks in DMSO, and are mixed to correct concentration prior to use. The mice are imaged in 5 minute increments for a total of 30 min, with a peak signal at 25 minutes post injection.

Glucose (GAz4) Uptake Imaging

Fast luciferase reporter mice for 16-18 hours over night. At the beginning of the fast, pre-inject mice with caged luciferin probe (CLP), i.p. 1.5 mM in 100 uL PBS+0.1%BSA. CLP solution is prepared from a stock solution 30 mM CLP in DMF. At the end of the fasting period, anaesthetize mice using isoflurane and image once using the IVIS to get background bioluminescence signal of CLP. While mice are still anaesthetized, i.p. inject 200 uL of the glucose probe (Gaz4) [38], 7.5 mM in PBS+0.1%BSA.

Image mice every 5 minutes for 35 minutes total.

Nicotinamide Riboside Uptake Imaging

Fast luciferase reporter mice for 16 hours over night. At the beginning of the fast, pre-inject mice with caged luciferin probe (CLP), i.p. 1.5 mM in 100 uL PBS+0.1%BSA. CLP solution is prepared from a stock solution 30 mM CLP in DMF. After 16 hour fasting period is over (16 hours post CLP injection), anaesthetize mice using isoflurane and image once using the IVIS to get background bioluminescence signal of CLP. While mice are still anaesthetized, oral gavage 100 µl nicotinamide riboside probe [169], 5 mM in PBS. The nicotinamide riboside probe is water soluble.

For fast-refeed experiment, inject mice with CLP two hours after beginning fast. At the end of fasting period, refeed mice for two hours then oral gavage and image nicotinamide riboside probe. This allows for imaging 16 hours after CLP injections.

Using IVIS system, acquire image every 5 min for 1 hour

Copper Imaging

Establish luciferase expressing tumors through our hydrodynamic injection method in FVB/NJ mice (strain #001800). Inject, through intraperitoneal injection, 100nmol of CCL1 probe[168] in 25ul DMSO 25ul PBS (50ul total). Using IVIS, image mice every 5 minutes for 45 min.

Iron Imaging

Establish luciferase expressing tumors through our hydrodynamic injection method in FVB/NJ mice (strain #001800). Inject, through intraperitoneal injection, 25nmol of ICL1 probe [170] in 25uL DMSO 75ul PBS (100ul total). Using IVIS, image every 5 minutes for 45 min.

ROS Imaging

Establish luciferase expressing tumors through our hydrodynamic injection method in FVB/NJ mice (strain #001800). Inject, through intraperitoneal injection, 0.5umol PCL1 probe [171] in 50ul 1:1 DMSO/PBS. Using IVIS, image mice every 5 minutes for 45 min.

Laser Ablation Inductively Coupled Plasma Mass Spectrometry (LA-ICP-MS)

Tumor bearing mice established using our standard protocol listed above. Monitored tumor growth and euthanized mice when full tumor burden was reached (6 weeks post hydrodynamic injection. Livers were perfused with PBS, cut into manageable pieces, and snap frozen. Frozen liver chunks were embedded in OCT, sectioned, and prepared for LA ICP-MS analysis as previously published [172].

AAV Generation

All adeno associated viruses were prepared, purified, and tittered according to our previously published method [153]
doi: 10.1074/jbc.M803510200

shRNA	**Target Gene**	**Target Sequence (Sense, 5' → 3')**
FATP5	mmFATP5	GTGGAAATCTCCTGCCATA
FATP2	mmFATP2	GGCGACATCTACTTCAACA
SCR	-	GATCGAATGTGTACTTCGA

KD experiments

Mice were injected through the lateral vein with 1x10^11-2x10^11 viral particles/uL in 250uL sterile PBS. Mice are given one week post injection to allow for knockdown to occur before proceeding to anther protocol.

Heavy water labeling

Animals with significant tumor burden (5 weeks post hydrodynamic injection) are intraperitoneal injected with a bolus of deuterated water, 35 uL of 100% D_2O per g of mouse. Mice are given 8% deuterated water in place of drinking water for 4 days, at which point the animals are sacrificed, livers are micro dissected for tumor nodules and snap frozen. The tumor containing liver samples are homogenized and the triglyceride fraction are isolated through thin layer chromatography. Samples are run on a GCMS to determine the deuterium enrichment in palmitate. Rates of *de novo lipogenesis* are then calculated using MIDA, as previously published [61,62]

Targeted Metabolomics

Tumor bearing livers were harvested from mice 6-7 weeks post hydrodynamic injection and dissected selecting for areas dense with tumor nodules. Samples were snap frozen for storage and were subsequently homogenized, lipid extracted, and run on a GC-MS/MS according to previously published protocol [173]
PNAS September 10, 2013 110 (37) 14912-14917; https://doi.org/10.1073/pnas.1310894110

Etomoxir administration

Mice were bottle trained for one week prior to the start of the experiment. Racemic (+)-Etomoxir (30 mg/kg/day) was administered to the treatment group in water for 5 weeks following hydrodynamic injection, and control mice were given untreated water in the same water bottles as the treatment group. Drinking water was acquired from the animal housing facility. Water treatments in both groups were replenished once per week and water consumption was recorded 3 times per week to ensure no difference between groups. Mice were put into the metabolic chambers for 3 days at the 1 week and 4 week time points to ensure the dosage of etomoxir had a phenotypic effect on metabolism throughout the treatment.

qPCR

Use Taqman quantitative PCR for all expression level measurements. Used Applied Biosystems TaqMan Fast Advanced Master Mix. All primer probes used are from Integrated DNA Technologies IDT and are pre-validated

Gene	Assay ID	Ref Seq #
PPIA	Mm.PT.39a.2.gs	NM_008907(1)
Slc27a2 (FATP2)	Mm.PT.58.12313563	NM_011978(1)
Slc27a5 (FATP5)	Mm.PT.58.5776058	NM_009512(1)
FASN	Mm.PT.58.14276063	NM_007988(1)

H&E

H&E staining was performed on either snap frozen tissues embedded in OCT or tissues fixed in 4% PFA embedded in paraffin.

Lipidomics heatmaps

Libraries Panda (pd), Numpy (np), Seaborn (sns), and Matplotlib.pyplot (plt) were loaded into python in order for certain functions to be used to construct the heatmap. Panda library was used to load our data into r using the function “pd.read_csv()”. Seaborn is unable to process datasets with missing values, so we went through an initial filtering process before generating the heatmap. Empty columns were removed using the “drop()” function, and missing values within our dataset were removed using the “drop.na()” function. It was necessary to assign “df1.iloc[:, 1]:” to the dataset after applying the function “np.log()” from the numpy library to calculate the natural log of all input elements. In order for the code to print the actions of the functions and visualize our work in a table, we finished the code chunk with “df1”. To view Data Frame 1 in a list, we coded “df1.columns”. We applied the same sets of functions to a different dataset, one that included only the main figure’s data: positive and negative data combined from a selected list of lipids.

It was then critical to use the “isin()” function to check if the values in the index in columns match or not, and filter out those that do not match. The Seaborn library generates the heatmap, but only works when the dataset is complete with no missing values. All acceptable data was made into a new dataset named col_used_df2. Further specification for the non-

matching values not to be displayed in the generation of any data visualization was deployed in code chunk 8.

The final heatmaps were built using the seaborn library, particularly the “sns.set()” function. Seaborn applied hierarchical clustering on our data which was normalized by fold change relative to control. Within this function, we specify the size of the figure using “figure.figsize” and we also set particular colors (coolwarm and white) to represent the heatmap correlations and gridlines. The widths of the bins are also set to 4 under linewidths of the sns.clustermap function. We used the matplotlib library to save the heatmaps: heatmap(df1) and heatmap(df2) were written to produce the output of the code.

Conclusion

In this dissertation, we aimed to investigate *in vivo* cancer metabolism using novel bioluminescent technology. We established three cancer mouse models, two hepatocellular carcinoma (HCC) models and one intrahepatic cholangiocarcinoma (ICC) model, where tumors exclusively express luciferase to leverage already existing bioluminescent probes and assess if there are any differences in metabolism. Because of the nature of this technology, we were able to make measurements in a noninvasive and longitudinal manner. We tested a total of six probes, three that were designed to measure glucose, fatty acid, and nicotinamide ribose uptake, and three designed to measure levels of iron, copper, and hydrogen peroxide. Our study showed differences in iron concentration and lipid uptake rates when comparing ICC to HCC. While we observed little to no lipid uptake in HCC, in line with the understanding that it is dependent on *de novo* lipogenesis (DNL) to acquire lipids for growth and survival, ICC maintained high levels of fatty acid uptake.

Not only do we see a difference in the origin of lipids used for tumor survival between ICC and HCC, but also in the lipid composition of each tumor type. Using targeted lipidomics, we measured the levels of over 100 lipid species and observed ICC to have higher levels of free fatty acids, structural and signaling lipids, and fatty acids implicated in energy generation. Seemingly, each tumor was not only getting its lipids from a different source, but also handling the lipids differently, preferentially shunting lipids into specific pathways. ICC is a highly malignant tumor and we wanted to assess if this was partially due to downstream lipid metabolism. We targeted energy metabolism by pharmacologically inhibiting CPT1, a transporter that imports fatty acids into the mitochondria to undergo beta-oxidation. We did not observe a significant impact on tumor growth.

Continuing to explore the role of lipid uptake in ICC, we directly targeted the fatty acid transport protein (FATP) family, which has been implicated in protein mediated exogenous fatty acid uptake. Liver contains both FATP2 and FATP5, with FATP5 being liver specific. Through knock out and knock down experiments, we observed that FATP5, but not FATP2, was the main transporter importing fatty acids into tumor cells and its ablation significantly inhibited tumor growth. In a survival experiment, we allowed tumors to grow for 32 weeks and out of seven mice, only three had tumor grow-outs. In two of those three mice, we found the tumors upregulated FASN, seemingly to acquire fatty acids through DNL. This further established the essential role of FATP5 in exogenous fatty acid uptake and its potential as a therapeutic target for ICC and potentially other liver cancers that are dependent on exogenous fatty acid uptake.

References

1. DeBerardinis, R.J., and Thompson, C.B. (2012). Cellular metabolism and disease: what do metabolic outliers teach us? Cell *148*, 1132-1144. 10.1016/j.cell.2012.02.032.
2. McKnight, S.L. (2010). On getting there from here. Science *330*, 1338-1339. 10.1126/science.1199908.
3. Adrain, C. (2021). Systemic and cellular metabolism: the cause of and remedy for disease? Febs j *288*, 3624-3627. 10.1111/febs.16033.
4. Speakman, J.R. (2013). Measuring energy metabolism in the mouse - theoretical, practical, and analytical considerations. Front Physiol *4*, 34. 10.3389/fphys.2013.00034.
5. Judge, M.T., Wu, Y., Tayyari, F., Hattori, A., Glushka, J., Ito, T., Arnold, J., and Edison, A.S. (2019). Continuous in vivo Metabolism by NMR. Front Mol Biosci *6*, 26. 10.3389/fmolb.2019.00026.
6. Dobbins, R.L., and Malloy, C.R. (2003). Measuring in-vivo metabolism using nuclear magnetic resonance. Curr Opin Clin Nutr Metab Care *6*, 501-509. 10.1097/00075197-200309000-00003.
7. Hwang, J.H., and Choi, C.S. (2015). Use of in vivo magnetic resonance spectroscopy for studying metabolic diseases. Exp Mol Med *47*, e139. 10.1038/emm.2014.101.
8. van der Horst, G., and van der Pluijm, G. (2012). Preclinical models that illuminate the bone metastasis cascade. Recent Results Cancer Res *192*, 1-31. 10.1007/978-3-642-21892-7_1.
9. O'Neill, K., Lyons, S.K., Gallagher, W.M., Curran, K.M., and Byrne, A.T. (2010). Bioluminescent imaging: a critical tool in pre-clinical oncology research. J Pathol *220*, 317-327. 10.1002/path.2656.
10. Mezzanotte, L., van 't Root, M., Karatas, H., Goun, E.A., and Löwik, C. (2017). In Vivo Molecular Bioluminescence Imaging: New Tools and Applications. Trends Biotechnol *35*, 640-652. 10.1016/j.tibtech.2017.03.012.
11. Dothager, R.S., Flentie, K., Moss, B., Pan, M.H., Kesarwala, A., and Piwnica-Worms, D. (2009). Advances in bioluminescence imaging of live animal models. Curr Opin Biotechnol *20*, 45-53. 10.1016/j.copbio.2009.01.007.
12. Zinn, K.R., Chaudhuri, T.R., Szafran, A.A., O'Quinn, D., Weaver, C., Dugger, K., Lamar, D., Kesterson, R.A., Wang, X., and Frank, S.J. (2008). Noninvasive bioluminescence imaging in small animals. Ilar j *49*, 103-115. 10.1093/ilar.49.1.103.
13. Tamulevicius, P., and Streffer, C. (1995). Metabolic imaging in tumours by means of bioluminescence. Br J Cancer *72*, 1102-1112. 10.1038/bjc.1995.472.
14. Vooijs, M., Jonkers, J., Lyons, S., and Berns, A. (2002). Noninvasive imaging of spontaneous retinoblastoma pathway-dependent tumors in mice. Cancer Res *62*, 1862-1867.
15. Wetterwald, A., van der Pluijm, G., Que, I., Sijmons, B., Buijs, J., Karperien, M., Löwik, C.W., Gautschi, E., Thalmann, G.N., and Cecchini, M.G. (2002). Optical imaging of cancer metastasis to bone marrow: a mouse model of minimal residual disease. Am J Pathol *160*, 1143-1153. 10.1016/s0002-9440(10)64934-6.
16. Tang, Y., Shah, K., Messerli, S.M., Snyder, E., Breakefield, X., and Weissleder, R. (2003). In vivo tracking of neural progenitor cell migration to glioblastomas. Hum Gene Ther *14*, 1247-1254. 10.1089/104303403767740786.
17. Benaron, D.A., Contag, P.R., and Contag, C.H. (1997). Imaging brain structure and function, infection and gene expression in the body using light. Philos Trans R Soc Lond B Biol Sci *352*, 755-761. 10.1098/rstb.1997.0059.
18. Sadikot, R.T., Jansen, E.D., Blackwell, T.R., Zoia, O., Yull, F., Christman, J.W., and Blackwell, T.S. (2001). High-dose dexamethasone accentuates nuclear factor-kappa b activation in endotoxin-treated mice. Am J Respir Crit Care Med *164*, 873-878. 10.1164/ajrccm.164.5.2008059.

19. Contag, C.H., Spilman, S.D., Contag, P.R., Oshiro, M., Eames, B., Dennery, P., Stevenson, D.K., and Benaron, D.A. (1997). Visualizing gene expression in living mammals using a bioluminescent reporter. Photochem Photobiol *66*, 523-531. 10.1111/j.1751-1097.1997.tb03184.x.
20. Contag, C.H., Jenkins, D., Contag, P.R., and Negrin, R.S. (2000). Use of reporter genes for optical measurements of neoplastic disease in vivo. Neoplasia *2*, 41-52. 10.1038/sj.neo.7900079.
21. Contag, C.H., and Bachmann, M.H. (2002). Advances in in vivo bioluminescence imaging of gene expression. Annu Rev Biomed Eng *4*, 235-260. 10.1146/annurev.bioeng.4.111901.093336.
22. Ray, P., De, A., Min, J.J., Tsien, R.Y., and Gambhir, S.S. (2004). Imaging tri-fusion multimodality reporter gene expression in living subjects. Cancer Res *64*, 1323-1330. 10.1158/0008-5472.can-03-1816.
23. Contag, C.H., Contag, P.R., Mullins, J.I., Spilman, S.D., Stevenson, D.K., and Benaron, D.A. (1995). Photonic detection of bacterial pathogens in living hosts. Mol Microbiol *18*, 593-603. 10.1111/j.1365-2958.1995.mmi_18040593.x.
24. Rocchetta, H.L., Boylan, C.J., Foley, J.W., Iversen, P.W., LeTourneau, D.L., McMillian, C.L., Contag, P.R., Jenkins, D.E., and Parr, T.R., Jr. (2001). Validation of a noninvasive, real-time imaging technology using bioluminescent Escherichia coli in the neutropenic mouse thigh model of infection. Antimicrob Agents Chemother *45*, 129-137. 10.1128/aac.45.1.129-137.2001.
25. Francis, K.P., Joh, D., Bellinger-Kawahara, C., Hawkinson, M.J., Purchio, T.F., and Contag, P.R. (2000). Monitoring bioluminescent Staphylococcus aureus infections in living mice using a novel luxABCDE construct. Infect Immun *68*, 3594-3600. 10.1128/iai.68.6.3594-3600.2000.
26. Francis, K.P., Yu, J., Bellinger-Kawahara, C., Joh, D., Hawkinson, M.J., Xiao, G., Purchio, T.F., Caparon, M.G., Lipsitch, M., and Contag, P.R. (2001). Visualizing pneumococcal infections in the lungs of live mice using bioluminescent Streptococcus pneumoniae transformed with a novel gram-positive lux transposon. Infect Immun *69*, 3350-3358. 10.1128/iai.69.5.3350-3358.2001.
27. Contag, P.R., Olomu, I.N., Stevenson, D.K., and Contag, C.H. (1998). Bioluminescent indicators in living mammals. Nat Med *4*, 245-247. 10.1038/nm0298-245.
28. Rehemtulla, A., Stegman, L.D., Cardozo, S.J., Gupta, S., Hall, D.E., Contag, C.H., and Ross, B.D. (2000). Rapid and quantitative assessment of cancer treatment response using in vivo bioluminescence imaging. Neoplasia *2*, 491-495. 10.1038/sj.neo.7900121.
29. Chewning, J.H., Dugger, K.J., Chaudhuri, T.R., Zinn, K.R., and Weaver, C.T. (2009). Bioluminescence-based visualization of CD4 T cell dynamics using a T lineage-specific luciferase transgenic model. BMC Immunol *10*, 44. 10.1186/1471-2172-10-44.
30. Guo, Y., Wang, B., Chen, Y., Liang, M., Wang, H., Wang, C., Liang, H., Zhou, Y., Xi, J., Ci, L., et al. (2021). A bioluminescence reporter mouse strain for in vivo imaging of CD8(+) T cell localization and function. Biochem Biophys Res Commun *581*, 12-19. 10.1016/j.bbrc.2021.10.022.
31. Bettano, K., Zielstorff, M., Sevilla, R., Yang, R., Zhou, H., Rosahl, T., Zhang-Hoover, J., Moy, L.Y., and Zhang, W. (2022). A bioluminescence reporter mouse model for visualizing and quantifying CD8+ T cells in vivo. Neoplasia *27*, 100781. 10.1016/j.neo.2022.100781.
32. Weinberg, R.A. (2014). Coming full circle-from endless complexity to simplicity and back again. Cell *157*, 267-271. 10.1016/j.cell.2014.03.004.
33. Hanahan, D., and Weinberg, R.A. (2000). The hallmarks of cancer. Cell *100*, 57-70. 10.1016/s0092-8674(00)81683-9.
34. Hanahan, D., and Weinberg, R.A. (2011). Hallmarks of cancer: the next generation. Cell *144*, 646-674. 10.1016/j.cell.2011.02.013.
35. Martínez-Reyes, I., and Chandel, N.S. (2021). Cancer metabolism: looking forward. Nat Rev Cancer *21*, 669-680. 10.1038/s41568-021-00378-6.
36. Liberti, M.V., and Locasale, J.W. (2016). The Warburg Effect: How Does it Benefit Cancer Cells? Trends Biochem Sci *41*, 211-218. 10.1016/j.tibs.2015.12.001.

37. DeBerardinis, R.J., and Chandel, N.S. (2020). We need to talk about the Warburg effect. Nat Metab *2*, 127-129. 10.1038/s42255-020-0172-2.
38. Maric, T., Mikhaylov, G., Khodakivskyi, P., Bazhin, A., Sinisi, R., Bonhoure, N., Yevtodiyenko, A., Jones, A., Muhunthan, V., Abdelhady, G., et al. (2019). Bioluminescent-based imaging and quantification of glucose uptake in vivo. Nat Methods *16*, 526-532. 10.1038/s41592-019-0421-z.
39. Su, T.A., Bruemmer, K.J., and Chang, C.J. (2019). Caged luciferins for bioluminescent activity-based sensing. Curr Opin Biotechnol *60*, 198-204. 10.1016/j.copbio.2019.05.002.
40. Snaebjornsson, M.T., Janaki-Raman, S., and Schulze, A. (2020). Greasing the Wheels of the Cancer Machine: The Role of Lipid Metabolism in Cancer. Cell Metab *31*, 62-76. 10.1016/j.cmet.2019.11.010.
41. Hay, N. (2016). Reprogramming glucose metabolism in cancer: can it be exploited for cancer therapy? Nat Rev Cancer *16*, 635-649. 10.1038/nrc.2016.77.
42. Adekola, K., Rosen, S.T., and Shanmugam, M. (2012). Glucose transporters in cancer metabolism. Curr Opin Oncol *24*, 650-654. 10.1097/CCO.0b013e328356da72.
43. Ancey, P.B., Contat, C., and Meylan, E. (2018). Glucose transporters in cancer - from tumor cells to the tumor microenvironment. Febs j *285*, 2926-2943. 10.1111/febs.14577.
44. Pliszka, M., and Szablewski, L. (2021). Glucose Transporters as a Target for Anticancer Therapy. Cancers (Basel) *13*. 10.3390/cancers13164184.
45. Mehmel, M., Jovanović, N., and Spitz, U. (2020). Nicotinamide Riboside-The Current State of Research and Therapeutic Uses. Nutrients *12*. 10.3390/nu12061616.
46. Navas, L.E., and Carnero, A. (2021). NAD(+) metabolism, stemness, the immune response, and cancer. Signal Transduct Target Ther *6*, 2. 10.1038/s41392-020-00354-w.
47. Yaku, K., Okabe, K., Hikosaka, K., and Nakagawa, T. (2018). NAD Metabolism in Cancer Therapeutics. Front Oncol *8*, 622. 10.3389/fonc.2018.00622.
48. Kincaid, J.W., and Berger, N.A. (2020). NAD metabolism in aging and cancer. Exp Biol Med (Maywood) *245*, 1594-1614. 10.1177/1535370220929287.
49. Lelièvre, P., Sancey, L., Coll, J.L., Deniaud, A., and Busser, B. (2020). The Multifaceted Roles of Copper in Cancer: A Trace Metal Element with Dysregulated Metabolism, but Also a Target or a Bullet for Therapy. Cancers (Basel) *12*. 10.3390/cancers12123594.
50. Ge, E.J., Bush, A.I., Casini, A., Cobine, P.A., Cross, J.R., DeNicola, G.M., Dou, Q.P., Franz, K.J., Gohil, V.M., Gupta, S., et al. (2022). Connecting copper and cancer: from transition metal signalling to metalloplasia. Nat Rev Cancer *22*, 102-113. 10.1038/s41568-021-00417-2.
51. Wang, F., Jiao, P., Qi, M., Frezza, M., Dou, Q.P., and Yan, B. (2010). Turning tumor-promoting copper into an anti-cancer weapon via high-throughput chemistry. Curr Med Chem *17*, 2685-2698. 10.2174/092986710791859315.
52. Manz, D.H., Blanchette, N.L., Paul, B.T., Torti, F.M., and Torti, S.V. (2016). Iron and cancer: recent insights. Ann N Y Acad Sci *1368*, 149-161. 10.1111/nyas.13008.
53. Guo, Q., Li, L., Hou, S., Yuan, Z., Li, C., Zhang, W., Zheng, L., and Li, X. (2021). The Role of Iron in Cancer Progression. Front Oncol *11*, 778492. 10.3389/fonc.2021.778492.
54. Torti, S.V., and Torti, F.M. (2013). Iron and cancer: more ore to be mined. Nat Rev Cancer *13*, 342-355. 10.1038/nrc3495.
55. Liou, G.Y., and Storz, P. (2010). Reactive oxygen species in cancer. Free Radic Res *44*, 479-496. 10.3109/10715761003667554.
56. Sullivan, L.B., and Chandel, N.S. (2014). Mitochondrial reactive oxygen species and cancer. Cancer & Metabolism *2*, 17. 10.1186/2049-3002-2-17.
57. Aggarwal, V., Tuli, H.S., Varol, A., Thakral, F., Yerer, M.B., Sak, K., Varol, M., Jain, A., Khan, M.A., and Sethi, G. (2019). Role of Reactive Oxygen Species in Cancer Progression: Molecular Mechanisms and Recent Advancements. Biomolecules *9*. 10.3390/biom9110735.

58. Perillo, B., Di Donato, M., Pezone, A., Di Zazzo, E., Giovannelli, P., Galasso, G., Castoria, G., and Migliaccio, A. (2020). ROS in cancer therapy: the bright side of the moon. Exp Mol Med *52*, 192-203. 10.1038/s12276-020-0384-2.
59. Henkin, A.H., Cohen, A.S., Dubikovskaya, E.A., Park, H.M., Nikitin, G.F., Auzias, M.G., Kazantzis, M., Bertozzi, C.R., and Stahl, A. (2012). Real-time noninvasive imaging of fatty acid uptake in vivo. ACS Chem Biol *7*, 1884-1891. 10.1021/cb300194b.
60. Park, H.M., Russo, K.A., Karateev, G., Park, M., Dubikovskaya, E., Kriegsfeld, L.J., and Stahl, A. (2017). A System for In Vivo Imaging of Hepatic Free Fatty Acid Uptake. Gastroenterology *152*, 78-81 e72. 10.1053/j.gastro.2016.10.002.
61. Hellerstein, M.K., Christiansen, M., Kaempfer, S., Kletke, C., Wu, K., Reid, J.S., Mulligan, K., Hellerstein, N.S., and Shackleton, C.H. (1991). Measurement of de novo hepatic lipogenesis in humans using stable isotopes. J Clin Invest *87*, 1841-1852. 10.1172/jci115206.
62. Hellerstein, M.K., and Neese, R.A. (1992). Mass isotopomer distribution analysis: a technique for measuring biosynthesis and turnover of polymers. Am J Physiol *263*, E988-1001. 10.1152/ajpendo.1992.263.5.E988.
63. Dufner, D., and Previs, S.F. (2003). Measuring in vivo metabolism using heavy water. Curr Opin Clin Nutr Metab Care *6*, 511-517. 10.1097/00075197-200309000-00004.
64. Broekaert, D., and Fendt, S.M. (2019). Measuring In Vivo Tissue Metabolism Using (13)C Glucose Infusions in Mice. Methods Mol Biol *1862*, 67-82. 10.1007/978-1-4939-8769-6_5.
65. Patterson, B.W. (2002). Methods for measuring lipid metabolism in vivo. Curr Opin Clin Nutr Metab Care *5*, 475-479. 10.1097/00075197-200209000-00004.
66. Chen, X., and Calvisi, D.F. (2014). Hydrodynamic transfection for generation of novel mouse models for liver cancer research. Am J Pathol *184*, 912-923. 10.1016/j.ajpath.2013.12.002.
67. Fan, B., Malato, Y., Calvisi, D.F., Naqvi, S., Razumilava, N., Ribback, S., Gores, G.J., Dombrowski, F., Evert, M., Chen, X., and Willenbring, H. (2012). Cholangiocarcinomas can originate from hepatocytes in mice. J Clin Invest *122*, 2911-2915. 10.1172/jci63212.
68. Li, L., Che, L., Tharp, K.M., Park, H.M., Pilo, M.G., Cao, D., Cigliano, A., Latte, G., Xu, Z., Ribback, S., et al. (2016). Differential requirement for de novo lipogenesis in cholangiocarcinoma and hepatocellular carcinoma of mice and humans. Hepatology *63*, 1900-1913. 10.1002/hep.28508.
69. Ho, C., Wang, C., Mattu, S., Destefanis, G., Ladu, S., Delogu, S., Armbruster, J., Fan, L., Lee, S.A., Jiang, L., et al. (2012). AKT (v-akt murine thymoma viral oncogene homolog 1) and N-Ras (neuroblastoma ras viral oncogene homolog) coactivation in the mouse liver promotes rapid carcinogenesis by way of mTOR (mammalian target of rapamycin complex 1), FOXM1 (forkhead box M1)/SKP2, and c-Myc pathways. Hepatology *55*, 833-845. 10.1002/hep.24736.
70. Hu, J., Che, L., Li, L., Pilo, M.G., Cigliano, A., Ribback, S., Li, X., Latte, G., Mela, M., Evert, M., et al. (2016). Co-activation of AKT and c-Met triggers rapid hepatocellular carcinoma development via the mTORC1/FASN pathway in mice. Sci Rep *6*, 20484. 10.1038/srep20484.
71. O'Neil, R.G., Wu, L., and Mullani, N. (2005). Uptake of a fluorescent deoxyglucose analog (2-NBDG) in tumor cells. Mol Imaging Biol *7*, 388-392. 10.1007/s11307-005-0011-6.
72. Park, J., Lee, H.Y., Cho, M.H., and Park, S.B. (2007). Development of a cy3-labeled glucose bioprobe and its application in bioimaging and screening for anticancer agents. Angew Chem Int Ed Engl *46*, 2018-2022. 10.1002/anie.200604364.
73. Society, A.C. (2019). Cancer Facts & Figures 2019. Atlanta: American Cancer Society.
74. Mittal, S., and El-Serag, H.B. (2013). Epidemiology of hepatocellular carcinoma: consider the population. J Clin Gastroenterol *47 Suppl*, S2-6. 10.1097/MCG.0b013e3182872f29.
75. El-Serag, H.B. (2012). Epidemiology of viral hepatitis and hepatocellular carcinoma. Gastroenterology *142*, 1264-1273.e1261. 10.1053/j.gastro.2011.12.061.

76. Razumilava, N., and Gores, G.J. (2014). Cholangiocarcinoma. Lancet *383*, 2168-2179. 10.1016/s0140-6736(13)61903-0.
77. Rizvi, S., Borad, M.J., Patel, T., and Gores, G.J. (2014). Cholangiocarcinoma: molecular pathways and therapeutic opportunities. Semin Liver Dis *34*, 456-464. 10.1055/s-0034-1394144.
78. Chen, Z., Xie, H., Hu, M., Huang, T., Hu, Y., Sang, N., and Zhao, Y. (2020). Recent progress in treatment of hepatocellular carcinoma. Am J Cancer Res *10*, 2993-3036.
79. Kane, R.C., Farrell, A.T., Madabushi, R., Booth, B., Chattopadhyay, S., Sridhara, R., Justice, R., and Pazdur, R. (2009). Sorafenib for the treatment of unresectable hepatocellular carcinoma. Oncologist *14*, 95-100. 10.1634/theoncologist.2008-0185.
80. Kim, D.W., Talati, C., and Kim, R. (2017). Hepatocellular carcinoma (HCC): beyond sorafenib-chemotherapy. J Gastrointest Oncol *8*, 256-265. 10.21037/jgo.2016.09.07.
81. Llovet, J.M., Ricci, S., Mazzaferro, V., Hilgard, P., Gane, E., Blanc, J.F., de Oliveira, A.C., Santoro, A., Raoul, J.L., Forner, A., et al. (2008). Sorafenib in advanced hepatocellular carcinoma. N Engl J Med *359*, 378-390. 10.1056/NEJMoa0708857.
82. Bekki, Y., Von Ahrens, D., Takahashi, H., Schwartz, M., and Gunasekaran, G. (2021). Recurrent Intrahepatic Cholangiocarcinoma - Review. Front Oncol *11*, 776863. 10.3389/fonc.2021.776863.
83. Wang, K., Zhang, H., Xia, Y., Liu, J., and Shen, F. (2017). Surgical options for intrahepatic cholangiocarcinoma. Hepatobiliary Surg Nutr *6*, 79-90. 10.21037/hbsn.2017.01.06.
84. Luengo, A., Gui, D.Y., and Vander Heiden, M.G. (2017). Targeting Metabolism for Cancer Therapy. Cell Chem Biol *24*, 1161-1180. 10.1016/j.chembiol.2017.08.028.
85. Stine, Z.E., Schug, Z.T., Salvino, J.M., and Dang, C.V. (2022). Targeting cancer metabolism in the era of precision oncology. Nat Rev Drug Discov *21*, 141-162. 10.1038/s41573-021-00339-6.
86. Ward, P.S., and Thompson, C.B. (2012). Metabolic reprogramming: a cancer hallmark even warburg did not anticipate. Cancer Cell *21*, 297-308. 10.1016/j.ccr.2012.02.014.
87. Schulze, A., and Harris, A.L. (2012). How cancer metabolism is tuned for proliferation and vulnerable to disruption. Nature *491*, 364-373. 10.1038/nature11706.
88. Cantor, J.R., and Sabatini, D.M. (2012). Cancer cell metabolism: one hallmark, many faces. Cancer Discov *2*, 881-898. 10.1158/2159-8290.Cd-12-0345.
89. DeBerardinis, R.J., and Chandel, N.S. (2016). Fundamentals of cancer metabolism. Sci Adv *2*, e1600200. 10.1126/sciadv.1600200.
90. Munir, R., Lisec, J., Swinnen, J.V., and Zaidi, N. (2019). Lipid metabolism in cancer cells under metabolic stress. Br J Cancer *120*, 1090-1098. 10.1038/s41416-019-0451-4.
91. Broadfield, L.A., Pane, A.A., Talebi, A., Swinnen, J.V., and Fendt, S.M. (2021). Lipid metabolism in cancer: New perspectives and emerging mechanisms. Dev Cell *56*, 1363-1393. 10.1016/j.devcel.2021.04.013.
92. Santos, C.R., and Schulze, A. (2012). Lipid metabolism in cancer. Febs j *279*, 2610-2623. 10.1111/j.1742-4658.2012.08644.x.
93. Currie, E., Schulze, A., Zechner, R., Walther, T.C., and Farese, R.V., Jr. (2013). Cellular fatty acid metabolism and cancer. Cell Metab *18*, 153-161. 10.1016/j.cmet.2013.05.017.
94. Daniëls, V.W., Smans, K., Royaux, I., Chypre, M., Swinnen, J.V., and Zaidi, N. (2014). Cancer cells differentially activate and thrive on de novo lipid synthesis pathways in a low-lipid environment. PLoS One *9*, e106913. 10.1371/journal.pone.0106913.
95. Stoiber, K., Nagło, O., Pernpeintner, C., Zhang, S., Koeberle, A., Ulrich, M., Werz, O., Müller, R., Zahler, S., Lohmüller, T., et al. (2018). Targeting de novo lipogenesis as a novel approach in anti-cancer therapy. Br J Cancer *118*, 43-51. 10.1038/bjc.2017.374.
96. Fhu, C.W., and Ali, A. (2020). Fatty Acid Synthase: An Emerging Target in Cancer. Molecules *25*. 10.3390/molecules25173935.

97. Flavin, R., Peluso, S., Nguyen, P.L., and Loda, M. (2010). Fatty acid synthase as a potential therapeutic target in cancer. Future Oncol *6*, 551-562. 10.2217/fon.10.11.
98. Lupu, R., and Menendez, J.A. (2006). Pharmacological inhibitors of Fatty Acid Synthase (FASN)--catalyzed endogenous fatty acid biogenesis: a new family of anti-cancer agents? Curr Pharm Biotechnol *7*, 483-493. 10.2174/138920106779116928.
99. Grunt, T.W., Slany, A., Semkova, M., Colomer, R., López-Rodríguez, M.L., Wuczkowski, M., Wagner, R., Gerner, C., and Stübiger, G. (2020). Membrane disruption, but not metabolic rewiring, is the key mechanism of anticancer-action of FASN-inhibitors: a multi-omics analysis in ovarian cancer. Sci Rep *10*, 14877. 10.1038/s41598-020-71491-z.
100. Falchook, G., Infante, J., Arkenau, H.T., Patel, M.R., Dean, E., Borazanci, E., Brenner, A., Cook, N., Lopez, J., Pant, S., et al. (2021). First-in-human study of the safety, pharmacokinetics, and pharmacodynamics of first-in-class fatty acid synthase inhibitor TVB-2640 alone and with a taxane in advanced tumors. EClinicalMedicine *34*, 100797. 10.1016/j.eclinm.2021.100797.
101. Koundouros, N., and Poulogiannis, G. (2020). Reprogramming of fatty acid metabolism in cancer. Br J Cancer *122*, 4-22. 10.1038/s41416-019-0650-z.
102. Chen, M., and Huang, J. (2019). The expanded role of fatty acid metabolism in cancer: new aspects and targets. Precis Clin Med *2*, 183-191. 10.1093/pcmedi/pbz017.
103. Watt, M.J., Clark, A.K., Selth, L.A., Haynes, V.R., Lister, N., Rebello, R., Porter, L.H., Niranjan, B., Whitby, S.T., Lo, J., et al. (2019). Suppressing fatty acid uptake has therapeutic effects in preclinical models of prostate cancer. Sci Transl Med *11*. 10.1126/scitranslmed.aau5758.
104. Drury, J., Rychahou, P.G., He, D., Jafari, N., Wang, C., Lee, E.Y., Weiss, H.L., Evers, B.M., and Zaytseva, Y.Y. (2020). Inhibition of Fatty Acid Synthase Upregulates Expression of CD36 to Sustain Proliferation of Colorectal Cancer Cells. Front Oncol *10*, 1185. 10.3389/fonc.2020.01185.
105. Xu, H., Chen, Y., Gu, M., Liu, C., Chen, Q., Zhan, M., and Wang, Z. (2021). Fatty Acid Metabolism Reprogramming in Advanced Prostate Cancer. Metabolites *11*. 10.3390/metabo11110765.
106. Kanefuji, T., Yokoo, T., Suda, T., Abe, H., Kamimura, K., and Liu, D. (2014). Hemodynamics of a hydrodynamic injection. Mol Ther Methods Clin Dev *1*, 14029. 10.1038/mtm.2014.29.
107. Suda, T., Gao, X., Stolz, D.B., and Liu, D. (2007). Structural impact of hydrodynamic injection on mouse liver. Gene Ther *14*, 129-137. 10.1038/sj.gt.3302865.
108. Budker, V., Zhang, G., Knechtle, S., and Wolff, J.A. (1996). Naked DNA delivered intraportally expresses efficiently in hepatocytes. Gene Ther *3*, 593-598.
109. Maruyama, H., Higuchi, N., Nishikawa, Y., Kameda, S., Iino, N., Kazama, J.J., Takahashi, N., Sugawa, M., Hanawa, H., Tada, N., et al. (2002). High-level expression of naked DNA delivered to rat liver via tail vein injection. J Gene Med *4*, 333-341. 10.1002/jgm.281.
110. Zhang, X., Dong, X., Sawyer, G.J., Collins, L., and Fabre, J.W. (2004). Regional hydrodynamic gene delivery to the rat liver with physiological volumes of DNA solution. J Gene Med *6*, 693-703. 10.1002/jgm.595.
111. Eastman, S.J., Baskin, K.M., Hodges, B.L., Chu, Q., Gates, A., Dreusicke, R., Anderson, S., and Scheule, R.K. (2002). Development of catheter-based procedures for transducing the isolated rabbit liver with plasmid DNA. Hum Gene Ther *13*, 2065-2077. 10.1089/10430340260395910.
112. Hen, G., Bor, A., Simchaev, V., Druyan, S., Yahav, S., Miao, C.H., and Friedman-Einat, M. (2006). Expression of foreign genes in chicks by hydrodynamics-based naked plasmid transfer in vivo. Domest Anim Endocrinol *30*, 135-143. 10.1016/j.domaniend.2005.06.002.
113. Yoshino, H., Hashizume, K., and Kobayashi, E. (2006). Naked plasmid DNA transfer to the porcine liver using rapid injection with large volume. Gene Ther *13*, 1696-1702. 10.1038/sj.gt.3302833.
114. Aliño, S.F., Herrero, M.J., Noguera, I., Dasí, F., and Sánchez, M. (2007). Pig liver gene therapy by noninvasive interventionist catheterism. Gene Ther *14*, 334-343. 10.1038/sj.gt.3302873.

115. Suda, T., and Liu, D. (2007). Hydrodynamic gene delivery: its principles and applications. Mol Ther *15*, 2063-2069. 10.1038/sj.mt.6300314.
116. Sendra, L., Herrero, M.J., and Aliño, S.F. (2018). Translational Advances of Hydrofection by Hydrodynamic Injection. Genes (Basel) *9*. 10.3390/genes9030136.
117. Niola, F., Dagnæs-Hansen, F., and Frödin, M. (2019). In Vivo Editing of the Adult Mouse Liver Using CRISPR/Cas9 and Hydrodynamic Tail Vein Injection. Methods Mol Biol *1961*, 329-341. 10.1007/978-1-4939-9170-9_20.
118. Xue, W., Chen, S., Yin, H., Tammela, T., Papagiannakopoulos, T., Joshi, N.S., Cai, W., Yang, G., Bronson, R., Crowley, D.G., et al. (2014). CRISPR-mediated direct mutation of cancer genes in the mouse liver. Nature *514*, 380-384. 10.1038/nature13589.
119. Huang, M., Sun, R., Wei, H., and Tian, Z. (2013). Simultaneous knockdown of multiple ligands of innate receptor NKG2D prevents natural killer cell-mediated fulminant hepatitis in mice. Hepatology *57*, 277-288. 10.1002/hep.25959.
120. Vakili, S., Ebrahimi, S.S., Sadeghi, A., Gorgani-Firuzjaee, S., Beigy, M., Pasalar, P., and Meshkani, R. (2013). Hydrodynamic-based delivery of PTP1B shRNA reduces plasma glucose levels in diabetic mice. Mol Med Rep *7*, 211-216. 10.3892/mmr.2012.1172.
121. Yokoo, T., Kamimura, K., Abe, H., Kobayashi, Y., Kanefuji, T., Ogawa, K., Goto, R., Oda, M., Suda, T., and Terai, S. (2016). Liver-targeted hydrodynamic gene therapy: Recent advances in the technique. World J Gastroenterol *22*, 8862-8868. 10.3748/wjg.v22.i40.8862.
122. Belcher, J.D., Vineyard, J.V., Bruzzone, C.M., Chen, C., Beckman, J.D., Nguyen, J., Steer, C.J., and Vercellotti, G.M. (2010). Heme oxygenase-1 gene delivery by Sleeping Beauty inhibits vascular stasis in a murine model of sickle cell disease. J Mol Med (Berl) *88*, 665-675. 10.1007/s00109-010-0613-6.
123. Turunen, T.A., Kurkipuro, J., Heikura, T., Vuorio, T., Hytönen, E., Izsvák, Z., and Ylä-Herttuala, S. (2016). Sleeping Beauty Transposon Vectors in Liver-directed Gene Delivery of LDLR and VLDLR for Gene Therapy of Familial Hypercholesterolemia. Mol Ther *24*, 620-635. 10.1038/mt.2015.221.
124. Yang, P.L., Althage, A., Chung, J., and Chisari, F.V. (2002). Hydrodynamic injection of viral DNA: a mouse model of acute hepatitis B virus infection. Proc Natl Acad Sci U S A *99*, 13825-13830. 10.1073/pnas.202398599.
125. Bell, J.B., Podetz-Pedersen, K.M., Aronovich, E.L., Belur, L.R., McIvor, R.S., and Hackett, P.B. (2007). Preferential delivery of the Sleeping Beauty transposon system to livers of mice by hydrodynamic injection. Nat Protoc *2*, 3153-3165. 10.1038/nprot.2007.471.
126. Hackett, P.B., Jr., Aronovich, E.L., Hunter, D., Urness, M., Bell, J.B., Kass, S.J., Cooper, L.J., and McIvor, S. (2011). Efficacy and safety of Sleeping Beauty transposon-mediated gene transfer in preclinical animal studies. Curr Gene Ther *11*, 341-349. 10.2174/156652311797415827.
127. Carlson, C.M., Frandsen, J.L., Kirchhof, N., McIvor, R.S., and Largaespada, D.A. (2005). Somatic integration of an oncogene-harboring Sleeping Beauty transposon models liver tumor development in the mouse. Proc Natl Acad Sci U S A *102*, 17059-17064. 10.1073/pnas.0502974102.
128. Schaffer, J.E., and Lodish, H.F. (1994). Expression cloning and characterization of a novel adipocyte long chain fatty acid transport protein. Cell *79*, 427-436. 10.1016/0092-8674(94)90252-6.
129. Hirsch, D., Stahl, A., and Lodish, H.F. (1998). A family of fatty acid transporters conserved from mycobacterium to man. Proc Natl Acad Sci U S A *95*, 8625-8629. 10.1073/pnas.95.15.8625.
130. Huang, J., Zhu, R., and Shi, D. (2021). The role of FATP1 in lipid accumulation: a review. Mol Cell Biochem *476*, 1897-1903. 10.1007/s11010-021-04057-w.

131. Wu, Q., Ortegon, A.M., Tsang, B., Doege, H., Feingold, K.R., and Stahl, A. (2006). FATP1 is an insulin-sensitive fatty acid transporter involved in diet-induced obesity. Mol Cell Biol *26*, 3455-3467. 10.1128/mcb.26.9.3455-3467.2006.
132. Zhang, M., Di Martino, J.S., Bowman, R.L., Campbell, N.R., Baksh, S.C., Simon-Vermot, T., Kim, I.S., Haldeman, P., Mondal, C., Yong-Gonzales, V., et al. (2018). Adipocyte-Derived Lipids Mediate Melanoma Progression via FATP Proteins. Cancer Discov *8*, 1006-1025. 10.1158/2159-8290.Cd-17-1371.
133. Qiu, P., Wang, H., Zhang, M., Zhang, M., Peng, R., Zhao, Q., and Liu, J. (2020). FATP2-targeted therapies - A role beyond fatty liver disease. Pharmacol Res *161*, 105228. 10.1016/j.phrs.2020.105228.
134. Falcon, A., Doege, H., Fluitt, A., Tsang, B., Watson, N., Kay, M.A., and Stahl, A. (2010). FATP2 is a hepatic fatty acid transporter and peroxisomal very long-chain acyl-CoA synthetase. Am J Physiol Endocrinol Metab *299*, E384-393. 10.1152/ajpendo.00226.2010.
135. Khan, S., Gaivin, R., Abramovich, C., Boylan, M., Calles, J., and Schelling, J.R. (2020). Fatty acid transport protein-2 regulates glycemic control and diabetic kidney disease progression. JCI Insight *5*. 10.1172/jci.insight.136845.
136. Veglia, F., Tyurin, V.A., Blasi, M., De Leo, A., Kossenkov, A.V., Donthireddy, L., To, T.K.J., Schug, Z., Basu, S., Wang, F., et al. (2019). Fatty acid transport protein 2 reprograms neutrophils in cancer. Nature *569*, 73-78. 10.1038/s41586-019-1118-2.
137. Alicea, G.M., Rebecca, V.W., Goldman, A.R., Fane, M.E., Douglass, S.M., Behera, R., Webster, M.R., Kugel, C.H., 3rd, Ecker, B.L., Caino, M.C., et al. (2020). Changes in Aged Fibroblast Lipid Metabolism Induce Age-Dependent Melanoma Cell Resistance to Targeted Therapy via the Fatty Acid Transporter FATP2. Cancer Discov *10*, 1282-1295. 10.1158/2159-8290.Cd-20-0329.
138. Li, S., Zhang, Z., Lai, W.F., Cui, L., and Zhu, X. (2020). How to overcome the side effects of tumor immunotherapy. Biomed Pharmacother *130*, 110639. 10.1016/j.biopha.2020.110639.
139. Khan, S., Cabral, P.D., Schilling, W.P., Schmidt, Z.W., Uddin, A.N., Gingras, A., Madhavan, S.M., Garvin, J.L., and Schelling, J.R. (2018). Kidney Proximal Tubule Lipoapoptosis Is Regulated by Fatty Acid Transporter-2 (FATP2). J Am Soc Nephrol *29*, 81-91. 10.1681/asn.2017030314.
140. Anderson, C.M., and Stahl, A. (2013). SLC27 fatty acid transport proteins. Mol Aspects Med *34*, 516-528. 10.1016/j.mam.2012.07.010.
141. Pei, Z., Fraisl, P., Berger, J., Jia, Z., Forss-Petter, S., and Watkins, P.A. (2004). Mouse very long-chain Acyl-CoA synthetase 3/fatty acid transport protein 3 catalyzes fatty acid activation but not fatty acid transport in MA-10 cells. J Biol Chem *279*, 54454-54462. 10.1074/jbc.M410091200.
142. Herrmann, T., van der Hoeven, F., Grone, H.J., Stewart, A.F., Langbein, L., Kaiser, I., Liebisch, G., Gosch, I., Buchkremer, F., Drobnik, W., et al. (2003). Mice with targeted disruption of the fatty acid transport protein 4 (Fatp 4, Slc27a4) gene show features of lethal restrictive dermopathy. J Cell Biol *161*, 1105-1115. 10.1083/jcb.200207080.
143. Gimeno, R.E., Hirsch, D.J., Punreddy, S., Sun, Y., Ortegon, A.M., Wu, H., Daniels, T., Stricker-Krongrad, A., Lodish, H.F., and Stahl, A. (2003). Targeted deletion of fatty acid transport protein-4 results in early embryonic lethality. J Biol Chem *278*, 49512-49516. 10.1074/jbc.M309759200.
144. Stahl, A., Hirsch, D.J., Gimeno, R.E., Punreddy, S., Ge, P., Watson, N., Patel, S., Kotler, M., Raimondi, A., Tartaglia, L.A., and Lodish, H.F. (1999). Identification of the major intestinal fatty acid transport protein. Mol Cell *4*, 299-308. 10.1016/s1097-2765(00)80332-9.
145. Lin, M.H., and Khnykin, D. (2014). Fatty acid transporters in skin development, function and disease. Biochim Biophys Acta *1841*, 362-368. 10.1016/j.bbalip.2013.09.016.
146. Cifarelli, V., and Abumrad, N.A. (2018). Intestinal CD36 and Other Key Proteins of Lipid Utilization: Role in Absorption and Gut Homeostasis. Compr Physiol *8*, 493-507. 10.1002/cphy.c170026.

147. Czech, M.P. (2002). Fat targets for insulin signaling. Mol Cell *9*, 695-696. 10.1016/s1097-2765(02)00509-9.
148. Kim, Y.S., Jung, J., Jeong, H., Lee, J.H., Oh, H.E., Lee, E.S., and Choi, J.W. (2019). High Membranous Expression of Fatty Acid Transport Protein 4 Is Associated with Tumorigenesis and Tumor Progression in Clear Cell Renal Cell Carcinoma. Dis Markers *2019*, 5702026. 10.1155/2019/5702026.
149. Schmuth, M., Ortegon, A.M., Mao-Qiang, M., Elias, P.M., Feingold, K.R., and Stahl, A. (2005). Differential expression of fatty acid transport proteins in epidermis and skin appendages. J Invest Dermatol *125*, 1174-1181. 10.1111/j.0022-202X.2005.23934.x.
150. Doege, H., Baillie, R.A., Ortegon, A.M., Tsang, B., Wu, Q., Punreddy, S., Hirsch, D., Watson, N., Gimeno, R.E., and Stahl, A. (2006). Targeted deletion of FATP5 reveals multiple functions in liver metabolism: alterations in hepatic lipid homeostasis. Gastroenterology *130*, 1245-1258. 10.1053/j.gastro.2006.02.006.
151. Hubbard, B., Doege, H., Punreddy, S., Wu, H., Huang, X., Kaushik, V.K., Mozell, R.L., Byrnes, J.J., Stricker-Krongrad, A., Chou, C.J., et al. (2006). Mice deleted for fatty acid transport protein 5 have defective bile acid conjugation and are protected from obesity. Gastroenterology *130*, 1259-1269. 10.1053/j.gastro.2006.02.012.
152. Kumari, A., Pal Pathak, D., and Asthana, S. (2020). Bile acids mediated potential functional interaction between FXR and FATP5 in the regulation of Lipid Metabolism. Int J Biol Sci *16*, 2308-2322. 10.7150/ijbs.44774.
153. Doege, H., Grimm, D., Falcon, A., Tsang, B., Storm, T.A., Xu, H., Ortegon, A.M., Kazantzis, M., Kay, M.A., and Stahl, A. (2008). Silencing of hepatic fatty acid transporter protein 5 in vivo reverses diet-induced non-alcoholic fatty liver disease and improves hyperglycemia. J Biol Chem *283*, 22186-22192. 10.1074/jbc.M803510200.
154. Enooku, K., Tsutsumi, T., Kondo, M., Fujiwara, N., Sasako, T., Shibahara, J., Kado, A., Okushin, K., Fujinaga, H., Nakagomi, R., et al. (2020). Hepatic FATP5 expression is associated with histological progression and loss of hepatic fat in NAFLD patients. J Gastroenterol *55*, 227-243. 10.1007/s00535-019-01633-2.
155. Ruiz de Gauna, M., Biancaniello, F., González-Romero, F., Rodrigues, P.M., Lapitz, A., Gómez-Santos, B., Olaizola, P., Di Matteo, S., Aurrekoetxea, I., Labiano, I., et al. (2022). Cholangiocarcinoma progression depends on the uptake and metabolization of extracellular lipids. Hepatology. 10.1002/hep.32344.
156. Wang, M.D., Wang, N.Y., Zhang, H.L., Sun, L.Y., Xu, Q.R., Liang, L., Li, C., Huang, D.S., Zhu, H., and Yang, T. (2021). Fatty acid transport protein-5 (FATP5) deficiency enhances hepatocellular carcinoma progression and metastasis by reprogramming cellular energy metabolism and regulating the AMPK-mTOR signaling pathway. Oncogenesis *10*, 74. 10.1038/s41389-021-00364-5.
157. Geng, Q.S., Yang, M.J., Li, L.F., Shen, Z.B., Wang, L.H., Zheng, Y.Y., Xue, W.H., and Zhao, J. (2021). Over-Expression and Prognostic Significance of FATP5, as a New Biomarker, in Colorectal Carcinoma. Front Mol Biosci *8*, 770624. 10.3389/fmolb.2021.770624.
158. Zhou, W., Madrid, P., Fluitt, A., Stahl, A., and Xie, X.S. (2010). Development and validation of a high-throughput screening assay for human long-chain fatty acid transport proteins 4 and 5. J Biomol Screen *15*, 488-497. 10.1177/1087057110369700.
159. Nie, B., Park, H.M., Kazantzis, M., Lin, M., Henkin, A., Ng, S., Song, S., Chen, Y., Tran, H., Lai, R., et al. (2012). Specific bile acids inhibit hepatic fatty acid uptake in mice. Hepatology *56*, 1300-1310. 10.1002/hep.25797.
160. Ameer, F., Scandiuzzi, L., Hasnain, S., Kalbacher, H., and Zaidi, N. (2014). De novo lipogenesis in health and disease. Metabolism *63*, 895-902. 10.1016/j.metabol.2014.04.003.

161. Su, X., and Abumrad, N.A. (2009). Cellular fatty acid uptake: a pathway under construction. Trends Endocrinol Metab *20*, 72-77. 10.1016/j.tem.2008.11.001.
162. Yang, P.B., Hou, P.P., Liu, F.Y., Hong, W.B., Chen, H.Z., Sun, X.Y., Li, P., Zhang, Y., Ju, C.Y., Luo, L.J., et al. (2020). Blocking PPARγ interaction facilitates Nur77 interdiction of fatty acid uptake and suppresses breast cancer progression. Proc Natl Acad Sci U S A *117*, 27412-27422. 10.1073/pnas.2002997117.
163. Ladanyi, A., Mukherjee, A., Kenny, H.A., Johnson, A., Mitra, A.K., Sundaresan, S., Nieman, K.M., Pascual, G., Benitah, S.A., Montag, A., et al. (2018). Adipocyte-induced CD36 expression drives ovarian cancer progression and metastasis. Oncogene *37*, 2285-2301. 10.1038/s41388-017-0093-z.
164. Wang, J., and Li, Y. (2019). CD36 tango in cancer: signaling pathways and functions. Theranostics *9*, 4893-4908. 10.7150/thno.36037.
165. Liang, Y., Han, H., Liu, L., Duan, Y., Yang, X., Ma, C., Zhu, Y., Han, J., Li, X., and Chen, Y. (2018). CD36 plays a critical role in proliferation, migration and tamoxifen-inhibited growth of ER-positive breast cancer cells. Oncogenesis *7*, 98. 10.1038/s41389-018-0107-x.
166. Gyamfi, J., Yeo, J.H., Kwon, D., Min, B.S., Cha, Y.J., Koo, J.S., Jeong, J., Lee, J., and Choi, J. (2021). Interaction between CD36 and FABP4 modulates adipocyte-induced fatty acid import and metabolism in breast cancer. NPJ Breast Cancer *7*, 129. 10.1038/s41523-021-00324-7.
167. Feng, W.W., Wilkins, O., Bang, S., Ung, M., Li, J., An, J., Del Genio, C., Canfield, K., DiRenzo, J., Wells, W., et al. (2019). CD36-Mediated Metabolic Rewiring of Breast Cancer Cells Promotes Resistance to HER2-Targeted Therapies. Cell Rep *29*, 3405-3420.e3405. 10.1016/j.celrep.2019.11.008.
168. Heffern, M.C., Park, H.M., Au-Yeung, H.Y., Van de Bittner, G.C., Ackerman, C.M., Stahl, A., and Chang, C.J. (2016). In vivo bioluminescence imaging reveals copper deficiency in a murine model of nonalcoholic fatty liver disease. Proc Natl Acad Sci U S A *113*, 14219-14224. 10.1073/pnas.1613628113.
169. Maric, T. (2020). Development of novel tools for imaging of metabolic fluxes in vivo. 10.5075/epfl-thesis-7551.
170. Aron, A.T., Heffern, M.C., Lonergan, Z.R., Vander Wal, M.N., Blank, B.R., Spangler, B., Zhang, Y., Park, H.M., Stahl, A., Renslo, A.R., et al. (2017). In vivo bioluminescence imaging of labile iron accumulation in a murine model of Acinetobacter baumannii infection. Proc Natl Acad Sci U S A *114*, 12669-12674. 10.1073/pnas.1708747114.
171. Van de Bittner, G.C., Dubikovskaya, E.A., Bertozzi, C.R., and Chang, C.J. (2010). In vivo imaging of hydrogen peroxide production in a murine tumor model with a chemoselective bioluminescent reporter. Proc Natl Acad Sci U S A *107*, 21316-21321. 10.1073/pnas.1012864107.
172. Ackerman, C.M., Weber, P.K., Xiao, T., Thai, B., Kuo, T.J., Zhang, E., Pett-Ridge, J., and Chang, C.J. (2018). Multimodal LA-ICP-MS and nanoSIMS imaging enables copper mapping within photoreceptor megamitochondria in a zebrafish model of Menkes disease. Metallomics *10*, 474-485. 10.1039/c7mt00349h.
173. Benjamin, D.I., Cozzo, A., Ji, X., Roberts, L.S., Louie, S.M., Mulvihill, M.M., Luo, K., and Nomura, D.K. (2013). Ether lipid generating enzyme AGPS alters the balance of structural and signaling lipids to fuel cancer pathogenicity. Proc Natl Acad Sci U S A *110*, 14912-14917. 10.1073/pnas.1310894110.